1 **Asynchronous glacial dynamics of LGM mountain glaciers in Ikh Bogd massif of Gobi-Altai range,**
2 **southwestern Mongolia: Aspect control on glacier mass balance**

3 Purevmaa Khandsuren [1], Yeong Bae Seong [1] *, Hyun Hee Rhee [2], Cho-Hee Lee [1], Mehmet Akif Sarikaya[3], Jeong-
4 Sik Oh [4], Khadbaatar Sandag [5], Byung Yong Yu [6]

5 [1] Department of Geography, Korea University, Seoul 02841, Korea;
6 [2] Division of Glacial Environment Research, Korea Polar Research Institute, Incheon 21990, Korea;
7 [3] Istanbul Technical University, Eurasian Institute of Earth Sciences, Sarıyer-Istanbul, 34469, Turkey;
8 [4] Department of Geography, Kyungpook National University, Daegu 41566, Korea;
9 [5] Department of Geography, Mongolian National University of Education, Ulaanbaatar 210648, Mongolia;
10 [6] AMS laboratory, Korea Institute of Science and Technology, Seoul 02792, Korea;
11 Correspondence to: Yeong Bae Seong (ybseong@korea.ac.kr)

13 **Abstract**. Mountain glacier mass balance is affected by factors other than climate, such as topography, slope, and
14 aspect. In mid-latitude high mountain regions, the north-south aspect contrast can cause significant changes in
15 insolation and melt, resulting in local asynchrony in glacial dynamics. This study documents the asynchronous
16 response of two paleoglaciers in southwestern Mongolia to the local topoclimatic factors using ^{10}Be exposure age
17 dating and 2D ice surface modelling. ^{10}Be surface exposure age dating revealed that the Ikh Artsan south-facing valley
18 glacier culminated (M_{IA1}) at 20.1 ± 0.7 ka, coinciding with the gLGM. In contrast, the north-facing Jargalant
19 paleoglacier (M_{J1}) culminated at 17.2 ± 1.5 ka, around Heinrich 1 stadial and during the post-gLGM northern
20 hemisphere warming. Our temperature-index melt model predicts that ablation will be substantially lower on the north-
21 facing slope as it is exposed to less solar radiation and cooler temperatures than on the south-facing slope. Two-
22 dimensional ice surface modeling also revealed that the south-facing Ikh Artsan glacier abruptly retreated from its
23 maximum extent since 20 ka, but the Jargalant glacier on the shaded slope consistently advanced and thickened due
24 to reduced melt till 17 ka. The timings of the modelled glacier culmination are consistent within ±1σ of the ^{10}Be
25 exposure age results. Extremely old ages ranging from 636.2 ka to 35.9 ka were measured for the inner moraines in
26 the Jargalant cirque (M_{J2}-M_{J4}), suggesting a problem with inheritance from boulders eroded from the summit plateau.

28 **Keywords:** Glacier, late Quaternary, Mongolia, Ikh Bogd, ^{10}Be surface exposure dating, paleo-erosion surface,
29 uplifted peneplain, 2D ice surface modelling

31 **1.   INTRODUCTION**

32   Massive ice sheets or mountain glaciers respond to various climatic forcings that operate on wide geographic

33 scales from local to global. Winter precipitation and summer air temperature are generally considered the most critical

34 factors in controlling glacial mass balance and extent. Understanding the impact of climate on past glacial cycles

35 necessitates a thorough understanding of the timing and amplitude of glacial dynamics. The most recent planet-wide

36 glacial expansion occurred during the global Last Glacial maximum (gLGM) as a result of changes in major climate

37 forcings, e.g., reduced summer insolation, lower tropical sea surface temperatures, and low atmospheric CO_2 content.

38 The remnants of paleoglacial deposits of gLGM are the best preserved among all the ice ages. The gLGM has been

39 extensively studied to ascertain the late Pleistocene changes in ice volume, sea-level fluctuations, feedback on climate,

40 etc. The timing of gLGM has been established using both the marine (e.g., Shackleton, 1967; Shackleton, 2000;

41 Thompson et al., 2003; Skinner and Shackleton, 2005) and terrestrial (e.g., An et al., 1991; Wang et al., 2001; Jouzel

42 et al., 2007; Clark et al., 2009; Fletcher et al., 2010;) paleoclimatic proxies. Based on proxy records, the timing of

43 gLGM is constrained between 26.5 and 19 ka, during which the ice sheets and mountain glaciers reached their

44 maximum and the global sea level was at its minimum (Clark et al., 2009).

45   The timing and extent of the maximum glaciation in many regions worldwide are poorly understood because

46 distinct ice masses respond differently to local and regional climatic conditions. New geochronological techniques

47 such as in situ cosmogenic surface exposure dating (e.g., Hughes et al., 2013; Heyman, 2014) permit reliable temporal

48 comparisons between the maximum advances of different mountain glaciers.

49   Evidence from mid-latitude glaciers reveals more complex behavior than that of synchronized 'global'

50 glaciations. In some parts of Asia, for example, the largest glacial extent occurred before Marine Isotope Stage (MIS)

51 2, >100 ka in the northeastern Tibetan plateau (Heyman et al., 2011a) and late MIS 5/MIS 4 in the Kanas lake, Chinese

52 Altai (Gribenski et al. 2018). In the Tian Shan (Koppes et al., 2008; Li et al., 2014; Blomdin et al., 2016), Altai

53 (Blomdin et al., 2018), Khangai (Rother et al., 2014; Smith et al., 2016; Batbaatar et al., 2018; Pötsch, 2017), and

54 Eastern Sayan, Khovsgol (Gillespie et al., 2008; Batbaatar and Gillespie, 2016) mountains, the largest glaciers dated

55 back to MIS 3, while the MIS 2 glaciers appeared to be smaller (Fig. 1). It is noteworthy that most of the MIS 3

56 advances are based on a few and/or widely scattered ages of moraine boulders (Blomdin et al., 2016; Gribenski et al.,

57 2018). On the other hand, in the Gichgeniyn range with arid climate conditions, the significant cirque glacier advanced

58 during MIS 1 (Batbaatar et al., 2018). These studies suggest that glaciers in continental interior Asia respond to

59 regional-scale climate fluctuation in different ways; hence, the last glacial maxima differed from place to place.

60 Equilibrium Line Altitude (ELA) depression of MIS 2 maximum varied ~100 to 1100 m from the arid to humid

61 continental environments. ELA depression estimated 800-1100 m in sub-humid regions (Russian Altai, Khangai,

62 Eastern Sayan, SE Tibetan plateau), 500-600 m in semi-arid Gobi Altai mountains, and 100-600 m in the arid northern

63 Tibetan plateau and Tian Shan (Batbaatar, 2018; see the locations in Fig. 1).

64   In addition to regional climate conditions, non-climatic factors may also control the local extent and dynamics

65 of glaciation. Topographic factors such as catchment morphology, valley width and length, slope, and aspect, can

66 influence glacier dynamics and affect the style of glaciation (Kirkbride and Winkler, 2012; Barr and Lovell, 2014).

67 Glacier mass balance varies with slope aspect, snow avalanche, and wind drifting snow. The north-south aspect

68   contrast in mid-latitude regions with steeper slopes, and higher relief can generate substantial differences in insolation
69   and melt. This difference may be more significant for cirque, small mountain glaciers, or niche glaciers than large
70   valley glaciers or ice caps (Evans and Cox, 2005).
71   Although spatio-temporal variations in the glacial extent in response to regional climate change have been
72   mentioned in numerous studies, the influence of topoclimatic factors has not been adequately explored. The present
73   study aims to evaluate how topographic shading affects fluctuations in the glacier surface mass balance and consequent
74   changes in glacier thickness and length (advance and retreat) using 2D ice surface model. The spatial and temporal
75   responses of contrastively oriented paleo glaciers to the aspect-driven microclimate are of particular interest to us. We
76   evaluated the response of two mountain glaciers, the south-facing Ikh Artsan glacier and the north facing Jargalant
77   glacier in southwest Mongolia (Jargalant; Fig. 1), to topo-climatic factors. Reliable temporal comparisons between
78   the maximum advances of the two mountain glaciers were made using in situ cosmogenic surface exposure dating
79   (e.g., Heyman, 2014; Hughes et al., 2013). This research will improve our understanding of how mid-latitude glaciers
80   respond to topographic changes.
81

82 ## 2. STUDY AREA

83 **2.1 General settings of the study area.**

84 The Gobi-Altai range, a ~800 km long NW-SE trending isolated arc of mountains, is bordered in the northwest by the

85 Mongolian Altai range and separated from the Khangai range by Valley of Lakes (Gobi Lakes Valley). Ikh Bogd

86 massif (Ikh Bogd means 'great saint' or 'great sacred mountain' in Mongolian) is located in the central Gobi-Altai

87 range. Ikh Bogd, Gobi-Altai range is one of the key sites for paleoglaciological, paleoenvironmental research in

88 landlocked arid, semi-arid central Asia.

89 This massif is over 50 km long, 25 km wide, and rises ~2 km above the surrounding arid piedmont. Terguun

90 Bogd (3957 m asl), the massif's highest peak, is also the highest point in the Gobi-Altai range (Fig. 1b). Ikh Bogd's

91 current stress regime is dominated by a network of thrust faults and sinistral strike-slip faults, that combine to form

92 transpressional pop-up structures (Cunningham et al., 1996; Bayasgalan et al., 1999; Vassallo et al., 2007; Vassallo

93 et al., 2011). The highest part (>3000 m) of the flat summit plateau consists mainly of granite, while lower parts are

94 mostly occupied by gneiss (EIC, 1981; Jolivet et al., 2007; Vassallo et al., 2011).

95 The flat summit plateau is thought to be a remnant of a formerly extensive Mesozoic erosion surface (Berkey

96 and Morris, 1924; Devyatkin, 1974; Jolivet et al., 2007), surviving most of the Cenozoic due to its rapid and recent

97 uplift after long-term quiescence (Jolivet et al., 2007). Accordingly, erosion in Ikh Bogd is limited to several deep

98 gorges. The summit plateau is well-preserved in unincised areas because of the young age of the massif and arid

99 regional climate (Vassallo et al., 2011).

100 Headwater systems of intermittent streams merge and turn into main streams, which later flow out of the

101 mountain front and transport abundant sediments into large alluvial fans. Alluvial fans from adjacent valleys coalesce

102 (forming bajadas) and stretch to huge endorheic intermontane basins like the Gobi Lakes Valley (Fig. 2). Numerous

103 prior investigations suggest that the summit plateau of the Ikh Bogd massif lacks Quaternary glacial landforms (e.g.,

104 Jolivet et al., 2007; Vasallo et al., 2011). However, some well-preserved moraine ridges have been identified and

105 mapped in some cirques of the neighboring massifs including Ikh Artsan, Jargalant (Batbaatar et al., 2018).

106

107

108 **2.2 Climate**

109 Ikh Bogd massif is in the cold Gobi Desert, with high amplitude in diurnal and annual temperatures. The

110 climate of the study area is characterized by a dry, cold winter with limited snowfall and hot summer with more than

111 65% yearly precipitation coming in summer (Batbaatar et al., 2018). Bayankhongor (Fig. 2), the nearest aimag center

112 to the study area (the largest unit of Mongolian province), is 140 km away and receives 190 mm of precipitation per

113 year (2005-2019 average, NAMHEM, 2020), while it drops to 100 mm (Yu et al., 2017, Fig. 2b, 2c, and 2d) near Orog

114 lake (1168 m a.s.l, Zhang et al., 2022). The closest weather stations to Ikh Bogd are Bayangobi (1540 m a.s.l) in the

115 south and Bogd (1240 m a.s.l) in the north. The long-term mean annual temperature measured as 3.2 °C in Bayangobi

116 and 4.4 °C in Bogd (Fig. 2c and 2d). The average January temperature was approximately -18 °C in both stations

117 (NAMHEM, 2020).

118   Ikh Bogd experiences long winter, a lower mean annual temperature (-10 °C), and higher precipitation (200
119   mm) than its surrounding regions (Fig. 2a, 2b). Even in summer, the temperature is mostly below 0 °C at altitudes
120   above 3800 m a.s.l in Ikh Bogd (Long-term monthly temperatures are calculated using a dry lapse rate of 9.8 °C/km
121   from nearby Bayangobi weather station; Supplementary 1). It begins to snow in the nearby Gobi Lakes Valley around
122   the end of September, although it melts quickly. Nonetheless, due to the relatively cold temperature, a thin snow cover
123   persists on the summit plateau of Ikh Bogd between the end of September and the middle of April. Occasionally,
124   precipitation in the form of snow occurs during the summer (Landsat imagery, Farr et al., 2007). Compared to the cool
125   summer of Ikh Bogd, surrounding areas have warm summers. The July temperature rises to about 21.8 °C in
126   Bayangobi and 23.0 °C in Bogd. (Fig. 2d; NAMHEM, 2020).

127   Strong Siberian high pressure prohibits the entrance of westerlies during winter, while westerlies and
128   southwesterlies are still effective during summer in the study area. The orientation and shape of mobile dunes
129   northwest of Orog lake record the direction of prevailing winds from the northwest (Yu et al., 2019; Mischke et al.,
130   2020; NAMHEM, 2020). Much colder than present-day winters and summers in Mongolia are consistent with the
131   strengthening of the winter high pressure over northern Eurasia. LGM summers were 1 to 7 °C colder than today in
132   Mongolia. The southward shift of westerly storm tracks should, therefore, contribute to the lower than present
133   precipitation values (Tarasov et al., 1999). Multi-proxy records indicate that the local LGM climate if the study area
134   was very dry and harsh (Yu et al., 2019).

3. METHODOLOGY

3.1. Field investigation and geomorphologic mapping

We conducted the fieldwork around the Mongolian Altai in July 2018. Prior to fieldwork, we identified glacial erosional and depositional landforms from the ALOS PALSAR DEM with 12.5 m resolution (JAXA/METI, 2007) and oblique imageries of © ArcGIS Earth and © Google Earth. Only two categories of glacial landforms could be identified and mapped from the satellite imageries and DEM analysis, the glacial cirques and hummocky moraines. Glacial cirques, with amphitheater-like glacial erosional landforms, were easily recognized around the highest mountain areas. Identification of hummocky moraine has been made from the previous studies (Batbaatar et al., 2018) and oblique imageries of © ArcGIS Earth and © Google Earth imagery, since the DEM is of insufficient resolution to show the hummocky topography clearly. The mapping was performed in a GIS environment and mapped on 30 m Shuttle Radar Topographic Mission (SRTM), satellite imagery of © Bing Maps and © ArcGIS Earth. Pre-identified moraines were confirmed during fieldwork. They were then categorized based on their stratigraphic position and separation between moraine ridges. The naming of landforms (e.g., valleys) in the research area was based on locality names from a 1:100000-scale topographic map of Mongolia (ALAMGCM, 1970) and a conversation with local herders.

3.2. Equilibrium Line Altitude

Ikh Bogd massif is unglaciated today. Furthermore, the nearest modern glaciers to the study area are in Otgontenger (Khangai) and Sutai (Mongolian Altai), which are approximately 350 to 550 km north and west of the Ikh Bogd massif, respectively. Thus, we could not calculate present ELAs or ELA depression; hence only ELAs for former glaciers (Ikh Artsan and Jargalant paleoglaciers) were estimated.

The THAR method may include a large error when glacier geometry is complex (Benn and Lehmkuhl 2000). Yet, it is more suitable for our study area because it has simple glacier morphology. A relatively lower value of THAR (Meierding 1982) is commonly used in previous studies of mid-latitude glaciers; however, a higher value is applicable according to glacier type or location. We also used a higher THAR ratio of 0.58 because the Ikh Bogd massif must have a higher ratio due to its arid environment during the last glaciation (Gillespie et al. 2008; Felauer et al., 2012; Lehmkuhl et al., 2018).

$$ELA = A_t + 0.58(A_h - A_t) \qquad (1)$$

where A_h and A_t are the headwall and toe altitudes, respectively.

A major problem exists in defining the headwall limit of a former glacier, which is very subjective and arbitrary (Porter 2001). The glacial headwall altitude was considered to be 1/3 of the altitude difference between the cirque floor and the top of the rock cliff, which was a similar ratio for schrund-lines estimation in White Mountains, New Hampshire, USA (Goldthwait, 1970). Headwall altitude is extracted from ALOS PALSAR DEM with 12.5 m resolution (JAXA/METI, 2007). The altimetric error (vertical uncertainty) of the DEM is ~5-7 m (Chai et al., 2022, Ferreira and Cabral, 2022). Glacial toe altitude was measured in the field using GPS and confirmed with the altitude from the DEM.

3.3. Cosmogenic ^{10}Be surface exposure dating

172
173   We used cosmogenic ^{10}Be surface exposure dating based on the specific sampling procedure described below to
174   determine the timing of the last glacial advances in Ikh Bogd massif (Gosse and Phillips, 2001; Khandsuren et al.,
175   2019). We sampled quartz-rich granitic boulders on the moraine crests, which were not reworked and represented
176   single, distinguishable ice-marginal positions. We sampled boulders that are rooted in the upper flat surface of the
177   moraine crest and away from steep slopes to avoid post-depositional movement such as rolling and sliding downslope.
178   We excluded boulders smaller than 50 cm above ground level that are likely to have been buried, exhumed, or heavily
179   eroded. Samples were obtained by chisel and hammer from the top surfaces of boulders (less than 5 cm thick) to avoid
180   the edging effect. We sampled at least five boulders from each single moraine crest to statistically screen any outliers
181   such as inheritance or post-glaciation reworking.

182   We followed the laboratory works of Korea University Geochronology Laboratory (Seong et al., 2016), with
183   the revised procedure of Kohl and Nishiizumi (1992). Rock samples were crushed and sieved to obtain a
184   monomineralic quartz and avoid grain size dependency. Meteoric ^{10}Be and other contaminations were removed by
185   successive HF/HNO$_3$ leaching. Purified quartz grains (250~500 µm) were first spiked with ~1047.8 ppm concentrated
186   ^{9}Be carrier and then dissolved with HF/HNO$_3$. Fluorides were removed by perchloric (HClO$_4$) acid, while Be was
187   separated from other ions (cations/anions) using ion-exchange chromatography columns. Beryllium hydroxide was
188   recovered using ammonium hydroxides. Consequently, Be(OH)$_2$ gels were dried on high-temperature hotplates. They
189   were calcinated to be oxide forms in a furnace at higher temperatures (800 °C). BeO samples were mixed with
190   Niobium powder to get conductivity and targeted in aluminum target to be loaded into 6 MV tandem Accelerator Mass
191   Spectrometry (AMS) for ^{10}Be/^{9}Be ratio measurement in the Korea Institute of Science and Technology. ^{10}Be/^{9}Be ratios
192   for each sample were measured relative to the 07KNSTD standard sample 5-1 (Nishiizumi et al., 2007), having a
193   ^{10}Be/^{9}Be ratio of 2.71 x 10^{-11} ± 4.71 x 10^{-13} (calibrated error). The measured average ^{10}Be to ^{9}Be ratio of the processing
194   blank was 4.53 x 10^{-15} ± 1.6 x 10^{-15} (n=2). The exposure ages were calculated using Cronus-Earth online calculator v3
195   (Balco et al., 2008). ^{10}Be production rate scaling was based on the time-dependent and nuclide-specific LSDn scaling
196   (Lifton et al., 2014). Several studies on the last glacial history in continental central Asia (e.g. Rother et al., 2014,
197   Batbaatar et al., 2018) present ^{10}Be exposure ages referenced to other scaling methods. For a simple comparison, we
198   recalculated their exposure ages with LSDn scaling model. Errors of exposure ages were represented by external
199   uncertainty (1σ confidence level).

200   We tested the boulder populations to find outliers using the Chauvenet and Pierce criterion and normalized
201   deviation methods (Ross, 2003; Chauvenet, 1960, Batbaatar et al., 2018) before we assigned deglaciation ages of
202   moraine sequences. The idea behind using Chauvenet's criterion is to find a probability band centered on the mean of
203   a normal distribution containing all samples. Any data points that lie outside this probability band can be considered
204   to be outliers. In contrast, Peirce's criterion is based on Gaussian distribution, and the data point is rejected if its
205   deviation from the mean exceeds the maximum allowed deviation (calculated from the standard deviation of the group
206   and Peirce's criterion table). For the normalized deviation, a sample in groups was rejected if its normalized deviation
207   from the group mean (excluding the tested sample) was greater than two (Batbaatar et al., 2018). The sample was
208   excluded from the group if its exposure age was recognized as an outlier in any of these three methods. We also

209 calculated the reduced chi-square value and the relative uncertainty of the group (Balco, 2011) after rejecting outliers.

210 The arithmetic mean and group standard deviation were considered as a representation of the group age. However, we

211 also calculated the total uncertainty, including group standard deviation and external uncertainty (systematic

212 uncertainty) of each sample within the group (Batbaatar et al., 2018). We presented minimum exposure ages assuming

213 zero erosion because it has been negligible (at least for the sampled surface) since the boulders were deposited based

214 on field observations and considering almost negligible erosion in arid regions. We also performed boulder erosion

215 sensitivity tests on our exposure ages, using erosion rates of 1-4 mm kyr^{-1} (Blomdin et al., 2018). We omitted

216 corrections for snow cover and vegetation change due to the ephemeral winter snow cover at the elevations of the

217 sampled boulders (e.g., Gosse and Phillips, 2001) because modern winter snow cover (Oct-Apr) is very thin and no

218 tree cover exists due to aridity.

219 After rejecting the outliers, Welch's t-test statistics were also used to compare the exposure ages of distal

220 moraines of two groups ($M_{IA}1$ and M_{J1}). Welch's t-test assumes that the sample means being compared for two groups

221 are normally distributed and that the groups have unequal variances. The null hypothesis (H_0) states the means of the

222 two groups are same, while the alternative hypothesis (Ha) states that the means of two groups are unequal. We also

223 performed the t-test with the total uncertainty of the groups instead of group variances at a 0.05 significance level.

224 Since our study area is considered to be a well-preserved paleo peneplanation surface, the ^{10}Be concentration

225 of the flat summit plateau must be very high. If our sampled boulders have an "inherited" component from the summit

226 plateau, the apparent exposure age should significantly exceed the moraine deposition age. We assumed that the ^{10}Be

227 concentration from extremely old boulders could represent the concentration of the summit plateau itself. Hence, we

228 tried to calculate exposure age and the lowest erosion rate of the summit plateau using the highest measured ^{10}Be

229 concentration from the oldest moraine boulder. Therefore, we selected the highest point (3625 m, 44.6°N, 100.2°E)

230 between the Jargalant and Ikh Artsan cirques that is representable of the summit plateau. The minimum erosion rate

231 was calculated with the "Erosion rate calculator" of Cronus Earth V3.0.2 using elevation and geographical coordinate

232 of the selected point, sampling thickness, and ^{10}Be concentration of the oldest boulder, considering the shielding factor

233 as 1 (unshielded).

234

235

236 **3.4. The 2D ice surface modelling**

237

238 A 2D ice surface model covering 22-16 ka was used to examine the influence of aspect on glacier mass

239 balance and dynamics and to explain the empirical dating results. The model calculates glacier mass balance variation

240 and corresponding vertical changes in the glacial ice surface (3.4.1). Furthermore, it defines the glacier toe location

241 (3.4.2) relative to the changing ELA via ice thickening or thinning. Our simulation cannot model actual glaciers; rather,

242 it examines the possibility that variable melt rates could cause a significant difference in mass balance (Fig. 3).

243

244 **3.4.1 Glacial surface mass balance model: glacial thinning and thickening.**

245 Glacier mass balance (m) is determined by the summation of net ablation (a, see 3.4.1.1) and accumulation (c, see

246 3.4.1.2) over a stated period (t):

247 $m = a + c = \int_{t_1}^{t_2}(a + c)\, dt$ $\qquad$ (2)

248 To infer the net gain and loss of glacier mass along the longitudinal profile for both catchments, we calculated and

249 plotted the variations in June, July, August (JJA; see 3.4.1.1) melt and winter precipitation (i.e., snow through the

250 whole year; see 3.4.1.2) during 22-16 ka ago. The elevation of the profile was taken from DEM with 12.5 m spatial

251 resolution in 5 m spatial intervals. Site parameters and input parameters of this model are described in Tables 1 and 2.

252

253 **3.4.1.1 Glacier ablation: Temperature-index glacier melt model**

254 We assumed that the topography (aspect and slope) is the main factor producing a difference in daily incoming solar

255 radiation on the south- and north-facing slopes. The earth's surface receives more energy as the solar altitude angle (α)

256 is high (zenith angle and angle of incidence are low). The diurnal changes in solar altitude angle are caused by the

257 earth's rotation around its axis, which varies from morning to evening. At sunrise and sunset, the solar altitude angle

258 is 0 degrees, and it reaches its maximum value at noon. Accordingly, in the mountainous area of the northern

259 hemisphere, the south-facing slope receives the highest energy at noon. The north-facing slope, on the other hand,

260 receives little or no energy due to the topographic shading effect (Fig. 2e). Such a diurnal cycle of insolation would

261 result in a major variation in the yearly or long-term mass balance of mountain glaciers (by surface melt) flowing on

262 south- and north-facing slopes on a long-term scale.

263 **Calculating orbital parameters**

264 $\qquad$ Combined influence caused by the slow changes in axial tilt (obliquity), shape of the Earth's orbit

265 (eccentricity), and axial precession results in long-term cyclical changes in daily incoming solar radiation. First, we

266 computed long-term variations in orbital parameters such as obliquity, eccentricity, and longitude of the perihelion

267 (Berger and Loutre, 1991). These main orbital elements cause the long-term variation of solar declination (δ) that

268 produce seasonal variation in solar altitude at the given latitude. Then, the long-term variation of solar declination was

269 used to calculate the hour angle (ω), zenith angle (Z), and angle of incidence (θ) (Eq. 3-11). We calculated all values

270 above related to the orbital parameters in time-dependent manner (Fig. 3).

271 **Calculating hour angle**

272 $\qquad$ To define aspect-driven contrast in potential direct solar radiation between south-facing and north-facing

273 valleys, we calculated hourly insolation (Eq. 12) with the same input parameters, except for the topography (aspect

274 and slope; Fig. 3). We calculated cell-by-cell sunrise and sunset hour angles of given topography for each valley (Eqs.

275 3-9) and gave 15° of increment for every one hour to calculate the hourly insolation, starting from the sunrise hour

276 angle until it exceeds the sunset hour angle.

277

278 Sunrise and sunset hour angles on the inclined surface were calculated as a function of latitude, solar declination,

279 slope, and azimuth (Iqbal, 1963). Sunrise hour angle for horizontal surface:

280

281 $\omega_s = \cos^{-1}(-\tan\varphi\,\tan\delta)$ $\qquad$ (3)

282

283   The following equations give the sunrise and sunset hour angles on the surface oriented toward the east.

284      $\omega_{sr} = \min\left[\omega_s, \cos^{-1}\left(\frac{-xy-\sqrt{x^2-y^2+1}}{x^2+1}\right)\right]$ (4)

285

286      $\omega_{ss} = -\min\left[\omega_s, \cos^{-1}\left(\frac{-xy+\sqrt{x^2-y^2+1}}{x^2+1}\right)\right]$ (5)

287

288   The following equations give the sunrise and sunset hour angles on the surface oriented toward the west.

289      $\omega_{sr} = \min\left[\omega_s, \cos^{-1}\left(\frac{-xy+\sqrt{x^2-y^2+1}}{x^2+1}\right)\right]$ (6)

290      $\omega_{ss} = -\min\left[w_s, \cos^{-1}\left(\frac{-xy-\sqrt{x^2-y^2+1}}{x^2+1}\right)\right]$ (7)

291

292   where x and y are kinds of coefficient to make the equations above simpler (Eq. 1.6.7 of Iqbal, 1983).

293      $x = \frac{\cos\varphi}{\sin\gamma\,\tan\beta} + \frac{\sin\beta}{\tan\gamma}$ (4)

294

295      $y = \tan\delta\left(\frac{\sin\varphi}{\sin\gamma\,\tan\beta} - \frac{\cos\varphi}{\tan\gamma}\right)$ (5)

296

297   Equations 3-9 are for calculating hour angles in arbitrary surfaces, where ω_s is the sunrise hour angle for horizontal

298   surfaces, ω_{sr}, ω_{ss} is the sunrise and the sunset hour angles on the inclined surface, φ is the latitude, δ is the solar

299   declination angle, β is the slope inclination angle, and γ is the surface azimuth angle.

300

301   **Calculating zenith angle and angle of incidence**

302   Then, the local zenith angle (Z) and the angle of incidence (θ) were calculated using hour angles at one-hour

303   intervals (ω). The zenith angle is angle between sun rays and normal plane to the surface ($90°-\alpha$) and approximated

304   as a function of latitude, solar declination angle, and hour angle (Iqbal, 1983):

305

306      $Z = \sin\delta\,\sin\varphi + \cos\delta\,\cos\varphi\,\cos\omega$ (10)

307

308   and the angle of incidence on the arbitrary oriented surfaces is expressed as:

309

310      $\cos\theta = (\sin\varphi\,\cos\beta - \cos\varphi\,\sin\beta\,\cos\gamma)\sin\delta + (\cos\varphi\,\cos\beta + \sin\varphi\,\sin\beta\,\cos\gamma)\cos\delta\,\cos\omega + \cos\delta\,\sin\beta\,\sin\gamma\,\sin\omega$ (11)

311

312   where β is the slope inclination angle and γ is the surface azimuth angle.

313

314   **Calculating daily insolation and daily melt**

315   Hourly potential clear-sky direct solar radiation (I) was calculated as (Hock, 1999):

316      $I = I_0 \left(\frac{R_m}{R}\right)^2 \Psi_a^{\left(\frac{P}{P_0 \cos Z}\right)} \cos \theta$ (12)

317   where I_0 is solar constant (1368 W m^{-2};), $(R_m R^{-1})^2$ is the eccentricity correction factor of the Earth's orbit for the time

318   considered with R the instantaneous Sun-Earth distance, and R_m is the mean Sun-Earth distance, Ψ_a is the mean

319   atmospheric clear-sky transmissivity (Ψ_a=0.75: (Hock, 1998)), P_h is the atmospheric pressure (NOAA, 1976), P_0 is

320   the mean atmospheric pressure at sea level, Z is the local zenith angle, and θ is the angle of incidence between the

321   normal to the grid slope and the solar beam. Therefore, hourly insolation was summed into daily insolation for

322   corresponding day length (not for 24 hours; Fig. 3).

323

324   We calculated daily melt with following equation using daily insolation value (Eq. 12).

325

326      $a = \begin{cases} \left(\frac{1}{n}MF + a_{ice}\, I\right) T & : \ T > 0 \\ 0 & : \ T \leq 0 \end{cases}$ (13)

327   MF is a melt factor (mm d^{-1} °C^{-1}), a_{ice} is a radiation coefficient for ice surfaces, I is potential clear-sky direct solar

328   radiation at the ice surface (W m^{-2}), and T is the time-dependent monthly mean temperature (°C). Furthermore, we

329   integrated (summed) the daily melt into monthly and summer melt, which is the same with the total ablation in this

330   model (Fig. 3).

331

332   **Calculating time-dependent temperature.**

333   We calculated the time-dependent temperature of the study area in the following order:

334   1) Present-day monthly air temperatures (T) for both cirque headwall altitudes (3533.3 m in Jargalant, 3508.3 m in

335   Ikh Artsan) were calculated from the two nearest national weather stations using a summer adiabatic lapse rate of 8 °C

336   km^{-1} (Batbaatar et al., 2018). Bayangobi weather station (1540 m a.s.l.) is 27 km SE of the study region, and Bogd

337   (Horiult) weather station (1240 m a.s.l.) is 45 km NW (Fig. 2c).

338   2) We use only summer temperature because even today, monthly mean temperatures between August to May are less

339   than 0 °C, in which no melt occurs (NAMHEM, 2020). The long-term average of the extreme minimum temperature

340   at the mean glacial toe altitude (Ikh Artsan and Jargalant) is -5.2 °C (calculated from Bayankhongor 1874 m) a.s.l

341   using a lapse rate of 8 °C/km). The JJA mean temperature at the cirque headwall altitude was measured as 5.4 °C in

342   the Ikh Artsan valley and 3.5 °C in the Jargalant valley. We chose the value of 5.4 °C for the summer temperature of

343   the study area and used further calculations (see supplementary 1 file).

344   3) We obtained a time-dependent summer temperature since 22 ka. LGM summer temperature was easily calculated

345   by subtracting known LGM summer temperature anomaly (1–7 °C by Tarasov et al., 1999) from the present-day

346   temperature of the study area. The modern and LGM summer temperature of the study area (5.4 °C) was calibrated to

347   Greenland temperature data from the NGRIP ice core (Buizert et al., 2018) since 22 ka to obtain time-dependent

348   temperature variation (see supplementary 2 file).

349   4) LGM summer temperature anomalies ranging from -5.0 °C to -6 °C were applied to calculate glacial melt since 22

350   ka (see supplementary 2 file).

351

3.4.1.2 Glacier accumulation and snow data

352
353 Climatologies at high resolution for the Earth's land surface areas (CHELSA) provides a high resolution, downscaled
354 centennial climate model data since 20 ka. We used CHELSA-TraCE21k 1 km monthly precipitation time series
355 (Karger et al., 2017). Precipitation data between 22–20 ka was considered the same as 20 ka data. Only snowfall at
356 the mean altitude of each valley was considered glacial accumulation, which occurs when the monthly average
357 temperature is below 0 ℃.

358

3.4.2 Glacial advance and retreat model based on glacier thickness change

359
360 Finally, a simple 2D ice surface model reconstructed paleoglacier behavior for 22–16 ka in the study area. First, we
361 created small initial glacial surface profiles on both valleys using the 2D ice surface model developed by Benn and
362 Hulton (2010). We computed the ice surface elevation (ice thickness) along the profiles in both valleys with this model.
363 The model requires (1) assumed yield stress describing a glacier's basal shear stress and (2) a shape factor accounting
364 for the valley-drag effects. We plot the ice profile with 5 m spacing along the mid-line of each valley (Fig. 8d, e),
365 assuming constant basal shear stress of 50, 100, 150, 200, and 300 kPa. Shape factors were calculated perpendicular
366 to the profile with the same spacing with the profile. Subsequently, we calculated the glacier mass balance for 22–16
367 ka using our temperature-index melt model results and paleo snow accumulation data. Therefore, we applied
368 corresponding paleo mass balance values on the initial ice thickness profiles. Ikh Artsan and Jargalant glaciers are
369 mostly developed within a cirque. The maximum erosion related to the rotational movement beneath a cirque is closely
370 linked to the ELA for cirque glaciers (Dahl et al., 2003). Hence, in our model, the thickest ice surface related to the
371 maximum erosion was considered as ELA. Accordingly, variations in paleo ELAs were calculated regarding the ice
372 thickness change. Eventually, we used the simple quadratic function formula ($f(x)=ax^2 + bx + c$) to determine the
373 location of the glacial toe based on ELA and headwall altitude values (Benn and Hulton, 2010). With the glacial toe
374 location, we could evaluate the paleoglacier advance and retreat at any time of interest.

375

4. RESULTS

4.1 Field observation and moraine stratigraphy

In Ikh Bogd, late Quaternary glaciation is almost confined within the cirque, extensive valley glacier networks were absent. Glaciers in Ikh Artsan and Jargalant valleys were also restricted in the cirques and flowed shortly down to elevations of ~3000 m a.s.l. Jargalant valley merges to the largest valley on the northern flank called Bituut river valley (Fig. 1b). This large drainage only experienced glaciations in the form of short cirque-valley glaciers, like in Jargalant valley. The massif was limited to small single (no networking) cirque-valley glaciers is best explained by the arid climate of the interior of the Gobi Desert.

Ikh Artsan cirque is smaller and its glacial valley is shorter (~1 km) than Jargalant. The best-preserved moraines, with at least seven to eight morainal crests, occur in the Ikh Artsan cirque (Fig. 4; Fig. 6a; Batbaatar et al., 2018). The farthest moraine sequence (M_{IA1}) was distinguished by down-valley stratigraphic position and long flat ridge along the valley side (Fig. 4a). M_{IA1} moraine is composed of thick, unsorted glacial debris of different particle sizes (from silt to boulder) with huge granitic boulders at the top. Towards the left, the moraine is cut by an intermittent stream, forming a deep valley (Fig. 4).

The Jargalant paleoglacier has a larger accumulation area and length than Ikh Artsan glacier, advancing 1.5 km downvalley. The moraine stratigraphy of Jargalant hummocky moraine was quite complicated. The original moraine surface of the inner moraines has been dissected by longitudinal stream forming the parallel moraine mounds or elongated moraine ridges along the valley. In the field, we matched such uneroded surfaces (or ridges) with the similar elevation and assumed them as an individual sequence. Stratigraphically, we identified four different moraine sequences in the Jargalant complex (M_{J4}, M_{J3}, M_{J2}, and M_{J1}, from youngest to oldest; Figs. 5 and 6). M_{J4}, M_{J3}, and M_{J2} moraines are distinctively separated on the left side of the valley. Elongated moraine feature (M_{J3}, M_{J2}) at the right side of the valley looks like a single flow feature. However, we assumed that the original form of the moraine (separation) had been removed or reworked by the stream erosion (Fig. 6c). According to these matters, some moraine boundaries are still uncertain, hence we marked the boundary with dashed line (Fig. 5 and Fig. 6b, c). M_{J4} moraine lies between 3365–3410 m a.s.l, containing angular to sub-angular clast-supported pebble to boulders. Downvalley from the M_{J4} moraine, M_{J3} and M_{J2} moraines have been longitudinally dissected by stream channels and uneroded moraine surface forms elongated parallel moraine ridges with smooth matrix-supported flat tops and steep clast-supported sides. These streams are filled with the till and angular water-lain sediments. The oldest moraine (M_{J1}) was deposited further downvalley, consisting of a single moraine ridge with large granitic boulders lying on the finer matrix-supported deposit. We mapped the extent of the most distal moraine ridge from the lower end of M_{J2} moraine to the point where the slope changes abruptly. We speculate that this oldest moraine may have extended far enough to reach the Bituut valley; however, beyond this point, the moraine would have been reworked by post glacial processes and lateral erosion of Bituut river (Fig. 5 and Fig. 6b, c).

4.2. Late Pleistocene ELA reconstruction

412   LGM ELA was calculated for M_{IA1} and M_{J1} moraines (Table 3). We estimated the former ELA using a headwall

413   altitude of 3508–3532 m. The terminal moraine was also identified at an elevation of 3222 m a.s.l in the Ikh Artsan

414   valley. Accordingly, the ELA for the M_{IA1} moraine was 3388 m a.s.l. In contrast, a large terminal moraine was

415   deposited at 2998 m a.s.l in Jargalant valley. The ELA associated with M_{J1} moraine was 3308 m a.s.l., about 80 m

416   lower than M_{IA1} moraine.

417

418   **4.3. ^{10}Be surface exposure age dating**

419   We present 28 new ^{10}Be exposure ages obtained from the boulders associated with five different moraine sequences,

420   M_{IA1} in Ikh Artsan valley and M_{J1}, M_{J2}, $M_{J3,}$ and M_{J4} in Jargalant (Table 4; Fig. 6).

421   **Ikh Artsan valley:** seven granitic boulders (IAM001 to 007) sampled from the most distal moraine ridge ranged in

422   age between 21.2 ± 1.5 to 19.1 ± 1.3 ka. ^{10}Be exposure ages from this moraine sequence were well-clustered, and none

423   of the three methods (Chauvenet, Pierce, and standardized deviation) detected outliers. The moraine formation age

424   was found to be 20.1 ± 0.7 ka (20.1 ± 1.6 ka with total uncertainty), $R\chi^2$ was 0.29, and group relative uncertainty was

425   calculated as 4% (Fig. 7).

426   **Jargalant valley:** twenty-one granitic moraine boulders on the four moraine sequences were targeted. Five to seven

427   boulders from each moraine crest were sampled. Outliers were detected and rejected by Pierce and normalized

428   deviation criteria. Because, the results from Pierce and normalized deviation methods were consistent, however,

429   Chauvenet method could not recognize some outliers which were recognized by Pierce and normalized deviation

430   criterions. Exposure ages from the innermost M_{J4} moraine ranged from 636.2 ± 45.1 to 177.3 ± 11.3 ka. The oldest

431   age (JAM003, 636.2 ± 45.1 ka) was excluded, and the four remaining ^{10}Be exposure ages provided a mean age of

432   212.9 ± 45.9 ka (212.9 ± 47.9 ka with total uncertainty). Five boulders from the M_{J3} moraine ranged in age between

433   209.0 ± 26.1 to 35.9 ± 8.0 ka. The group mean age was calculated as 69.9 ± 39.4 ka (69.9 ± 41.5 ka with total

434   uncertainty) after rejecting an outlier of 209.0 ± 26.1 ka (JAM008). Boulders from the M_{J2} moraine yielded ages from

435   284.9 ± 18.4 to 162.1 ± 10.2 ka with a mean exposure age of 193.7 ± 36.7 ka (193.7 ± 41.1 ka with total uncertainty)

436   after rejecting the oldest age of 284.9 ± 18.4 ka (JAM012). Samples from the distal moraine of Jargalant valley (M_{J1})

437   ranged in age from 18.9 ± 1.7 to 10.6 ± 0.8 ka. The arithmetic mean age for this moraine sequence was 17.2 ± 1.5 ka

438   (17.2 ± 2.1 ka with total uncertainty) without the youngest age of 10.8 ± 0.5 ka (JAM016). The group was relatively

439   well clustered, and its relative uncertainty was 9% and $R\chi^2 = 1.18$ (Fig. 7). For erosion rates of 1-4 mm kyr^{-1}, an

440   exposure age of 10 ka calculated assuming zero erosion would underestimate the true age by 1-4% and an age of 20

441   ka by 2-7%. Samples with longer exposures (boulders with inheritance) older than 100 ka, were increasingly sensitive

442   to erosion; i.e., JAM10 (123.8 ka) had an impact, increasing ages with 12-125% for 1-4 mm kyr^{-1} and JAM03 (636.2

443   ka) was saturated even for 1 mm kyr^{-1} boulder erosion rate.

444   Our age dating results from most distal moraines of Ikh Artsan (20.1 ± 1.6 ka) and Jargalant (17.2 ± 2.1)

445   coincide within the narrow range (19.2-18.5 ka) as we apply total uncertainties to the group mean. However, T-test

446   reveals (T=3.928, P=0.001) that the exposure ages from the distal moraine of Ikh Artsan presented a statistically

447   significant difference from that of the Jargalant based on standard deviations (variance) of the two groups. Likewise,

448   the exposure ages of the two groups were different in 0.05 significance level (T=2.665, P=0.044) using total

449   uncertainties instead of the variance.

450   Boulders from inner moraines (M_{J4}, M_{J3}, and M_{J2}) presented older (~636.2–35.9 ka) exposure than the timing

451   of the maximum extent unlike morphostratigraphy-the inner moraines should be younger than the distal moraine (M_{J1}).

452   The unexpected, significant inheritance has been widely recognized around the globe in the previous studies (Ciner et

453   al., 2017; more references therein), possibly overestimating the real deposition age of moraine. We interpret that the

454   unexpected older exposure ages (~636.2–35.9 ka) from M_{J4}, M_{J3}, and M_{J2} moraines of Jargalant valley strongly imply

455   the inheritance from the summit plateau. These unusually old boulders are pieces of the summit plateau that were

456   transported onto the glacier surface by rockfall, which seems to happen in recent times as well. For temperate glacier,

457   rock fracturing occurs not only on the headwall above the glacier, but also within the bergschrund (bottom of the

458   headwall) by ice segregation. This kind of undermining (sapping) process or/and glacial debutressing would drive

459   consequent upper headwall collapse and give a large amount of rock supply to the glacier (Sanders et al., 2012; Table

460   4; Fig. 6b). ^{10}Be concentration of the oldest sample (JAM003 with ^{10}Be concentration of ~262.9×10^5) likely represents

461   nuclide concentration at the surface of the summit plateau. The production rate for the summit plateau (60.49 atoms

462   g^{-1} yr^{-1}) must be higher than the moraine samples (38.45 atoms g^{-1} yr^{-1}) due to its higher elevation (3625 m) than

463   sampling sites and 100% exposure (topographic shielding is 1) to cosmic-ray bombardment. With a high ^{10}Be

464   concentration of JAM003 and production rate of summit plateau (3625 m a.s.l), the assuming exposure age of the flat

465   summit plateau was calculated as 442.3 ± 29.8 ka, and the corresponding erosion rate was calculated as 1.23 ± 0.10

466   mm kyr^{-1}.

4.4. Results from 2D ice surface modelling

467

468   We ran the potential direct solar radiation model applying to a 12.5 m resolution DEM for a more realistic

469 comparison. The model suggests that the aspect largely affects the incoming potential clear-sky solar radiation. The

470 result approved that the south-facing slopes in mountainous regions receive more solar radiation than the north-facing

471 slope in our study area. At solar noon, the sun is always directly south in the northern hemisphere; hence southern

472 slopes of the mountainous area receive their maximum insolation. However, the orientations of the two valleys are

473 not true north or south. The azimuth of the Ikh Artsan is 247° (SSW), and for the Jargalant it is 40° (NNE). According

474 to the exact orientation, the peak of the daily insolation contrast between two valleys is calculated between 3 to 4 pm,

475 not at noon. The current June solstice incoming daily solar radiation in Ikh Artsan valley was 8527.34 WH m-2 and

476 7714.35 WH m-2 in Jargalant valley, whereas solar radiation was lower during 22 ka, 8460.07 WH m-2 in Ikh Artsan

477 and 7604.54 WH m-2 in Jargalant. Although both valleys received maximum insolation in the first to the middle half

478 of June, the maximum difference in incoming daily solar radiation occurred at the end of August. The main difference

479 in the daily incoming solar radiation ranges from 10–24% on summer days over the period of 22-16 ka. The spatial

480 distribution of potential direct solar radiation of the study area is given in Fig. 8. Typically, the total daily insolation

481 anomaly of summer solstice in 20 ka from present-day and integrated total daily insolation for 22-16 ka were described

482 on the 12.5 m grid cells (Fig. 8d, e). In the same way, 14% excess of total summer insolation was observed on the

483 southern slope during the modelling time interval of 22–16 ka (Fig. 8f; see supplementary 2 file).

484   For simplicity, the melt was calculated (Eq. 12) along specific profiles of Ikh Artsan and Jargalant valleys

485 (Fig. 8e, f). In accordance with the incoming solar radiation contrast, melt rates on south-facing slopes exceed those

486 on north-facing slopes, as would be expected. If modern glaciers existed in Ikh Bogd, the present-day summer melt

487 would be calculated as 4.0 m in Ikh Artsan valley and 3.7 m in Jargalant, respectively. This was a substantially high

488 melt rate in the arid, cool climate of the study area. The temperature-index melt model discovered that 5% of melt

489 excess in June solstice of any year between 22–16 ka was observed on the south-facing slope. Approximately 8% of

490 the difference in summer melt in any year was observed for 22–16 ka (Fig. 8f, see supplementary 2 file)

491   We run our 2D ice surface model for many times using different values of basal shear stress, LGM summer

492 temperature anomalies, and site temperature (Supplementary material 2). The cirque and valley dimensions reflect the

493 glacier size (including thickness), and the intensity of former glacial erosion (Barr and Spagnolo, 2015). The normal

494 stress acting on the glacier bed is mainly a result of the weight (thickness) of a glacier. Jargalant glacier is 2.7 times

495 larger in area than Ikh Artsan and twice as long in glacier length, forming a large, deep, and well-developed cirque.

496 According to the glacial valley size, we chose the higher basal shear stress for Jargalant valley (200 kPa) and the

497 smaller value for Ikh Artsan valley (100 kPa). LGM summer temperature anomalies ranging from -6 °C to -5 °C with

498 0.1 °C intervals were applied the same for both glaciers. Some previous studies suggest that temperature is lower on

499 the north-facing slopes at the same altitude. On the north-facing slope of Taibai, Qinling mountains, JJA monthly

500 mean temperature is measured 0.5–1 °C lower than on the south-facing slope in the altitude range of 1250–3750 m

501 (Tang and Fang, 2006). Therefore, we applied two different temperature values for north-facing Jargalant glacier; 1)

502 using the same present-day temperature with Ikh Artsan valley; and 2) using the lower present-day temperature for

503 Jargalant valley than Ikh Artsan.

504   **Case 1.** Applying the same present-day temperature: When we use the same present-day temperature and the
505   same LGM anomaly of -5.5 ℃, the modelled chronology of the maximum extents (20.2 ka) of two glaciers were
506   similar and consistent with the Ikh Artsan terminal moraine age dating result (20.1 ka). According to this model (case),
507   Jargalant moraine advanced maximally 20.1 ka and probably reached to Bituut valley.

508   **Case 2.** Applying the different present-day temperatures: For the Jargalant glacier, we applied lower present-
509   day temperature by -1 ℃ to -0 ℃ (at 0.1 ℃ interval) than Ikh Artsan. The run yielded different chronologies of
510   maximum ice expansions. Only a small temperature change between the south- and north-facing slope forced two
511   glaciers to behave asynchronously, the north-facing glacier got have 2.70–3.46 kyr of lag in the timing of the maximum
512   extent. When we applied -5.5 ℃ of LGM summer temperature anomaly and present-day summer temperature in
513   Jargalant 0.5 ℃ lower than in Ikh Artsan, Ikh Artsan glacier reached its maximum extent near 20.2 ka. In contrast,
514   the Jargalant glacier maximally advanced approximately at 17.1 ka. This result perfectly fits our [10]Be moraine age
515   dating results (20.1 ka and 17.2 ka).

516   **5. DISCUSSION**

517

518   **5.1. Asynchronous glaciation in mid-latitude ranges**

519   Recent glacial chronologies from mid-latitude mountain ranges in North Atlantic region document that Laurentide,
520   Scandinavian ice sheets and number of valley glaciers behaved synchronously, advancing to their maximum extent at
521   roughly the same time as the gLGM (26.5–19 ka). However, some experienced pre-LGM glacial maxima, while others
522   stagnated, re-advanced, continuously advanced even farther during the subsequent Heinrich Stadial 1 (HS-1, 17.5-
523   14.5 ka), displaying both inter-range and intra-range asynchrony (Laabs et al., 2009; Young et al., 2011; Licciardi and
524   Pierce 2018; Palacio et al., 2020).

525   In Europe, large-scale inter-range asynchrony (several tens of kyr) of last glacial termination was common.
526   Cosmogenic surface dating from the Alps and Turkey provides nearly synchronous last glacial maxima with the gLGM
527   (26.5–19 ka, MIS 2). Whereas other numerical dating techniques, including radiocarbon, U-series, and OSL, indicate
528   earlier local glacial maxima (80–30 ka, MIS 4 to MIS 3) in the Cantabrian Mountains, Pyrenees, Italian Apennines
529   and Pindus Mountains (e.g., Jimenez-Sanchez et al., 2013; Oliva et al., 2019). Another inter-range asynchrony was
530   observed in mountain glaciers of North America. They reached their maximum extent from as old as 25–24 ka for
531   some moraines and outwash in the Sierra Nevada to as young as 17–15 ka for some terminal moraines in the Rocky
532   Mountains but a clear central tendency exists with a mean of ~19.5 ka (Young et al., 2011; Laabs et al., 2020; Palacios
533   et al., 2020). Relatively younger ages (HS-1) across the mountains located in the higher latitude were interpreted as a
534   sign of glacial post-LGM culmination in response to increased delivery of westerly derived moisture which reached
535   the northern continental interior of the western U.S after the large ice sheets started to retreat (Licciardi et al., 2001;
536   Licciardi et al., 2004; Thackray, 2008). For instance, younger exposure ages of the last glacial maxima in the western
537   Uinta mountains, compared to mountain ranges farther east and north, reflected the influence of pluvial Lake
538   Bonneville after the recession of the Laurentide ice sheet to the north (Laabs et al., 2009).

539   Medium scale inter-range asynchrony (several thousand years) was observed in the Yellowstone plateau.
540   Terminal moraines dated to ~17 ka are common in valleys along the northeastern mountains (e.g., Eightmile, Chico,
541   Pine Creek, S.Fork Deep Creek, Cascade Canyon, and Gallatin) of the Great Yellowstone plateau. Glaciers in the
542   Teton Range (southwestern part of the plateau) have terminal moraine with the age of ~15 ka. Local LGM maxima
543   dated to ~19.8 to 18.2 ka in the western part of the plateau (Beartooth Uplift). Licciardi and Pierce (2018) suggested
544   that shifting orographic precipitation patterns due to the formation of ice dome and change in ice flow direction caused
545   asynchrony in the Great Yellowstone region.

546   Very few glacial chronologies, if any at all, record intra-range asynchrony during the most recent glacial
547   termination. Age dating results from some relatively well-studied mountain ranges (Wasatch, Uinta, Bighorn ranges
548   in North America) present intra-range asynchrony in glacial maxima in their various aspect (Laabs et al., 2020). Some
549   of them had LGM ages ranging from hundreds to thousands of years from valley to valley. In the Wasatch range,
550   terminal moraines dated to ~21.9 ka (Laabs and Munroe, 2016), ~20.8 ka, 17.3 ka (Laabs et al., 2011) in three western
551   valleys, 19.6 ka in the southwestern valley and 17.6 ka and 17.3 ka in the southeastern valleys (Quirk et al., 2020).
552   Similarly, the last glacial terminal moraine age difference of ~1 kyr was observed between the north-facing and south-

553 facing slope, Eastern Pyrenees (Delmas et al., 2011; Delmas et al., 2008). Even glaciers on the same oriented slope

554 contain some chronology difference. LGM moraine chronology from the three valleys on the east side of the central

555 Sawatch range varies from 22.3 ka to 19.9 ka (Young et al., 2011).

556 Nevertheless, we suggest that some internal, external, analytical uncertainties associated with sampling,

557 measurements, or/and statistical approach can cause the low magnitude of asynchrony in such small intra-range or

558 massif. Some studies have attributed intra-range asynchrony in terminal moraine ages to contrasting valley glacier

559 response times related to topography, ice dynamics and/or differences in glacier shape and hypsometry (Young et al.,

560 2011, Licciardi and Pierce, 2018). As mentioned above, large and medium-scale asynchrony in the mountain glaciers

561 across the North Atlantic region is mostly explained by precipitation distribution due to the relative location of the

562 moisture source area and atmospheric circulation contributed by topography. However, the intra-range or intra-massif

563 scale of asynchrony in the last glacial period needs further research to understand fully.

564

565

5.2. Inter-range asynchrony in ice expansion of last glacial cycle across the western Mongolia

567 Some [10]Be exposure ages of the glacial erratic from the mountain ranges nearby Ikh Bogd show the

568 significant glacial advances between LGM to the Holocene (Fig. 9). The largest ice extent was dated as ~22.0 ka on

569 the western flank of the Sutai (Batbaatar et al., 2018). On the other hand, the farthest ice expansion corresponds to

570 MIS 3 in the Khangai mountain range (Rother et al., 2014; Smith et al., 2016; Pötsch, 2017; Batbaatar et al., 2018).

571 In the Gichgeniyn mountains, Holocene (8–7 ka) glaciers advanced with a similar magnitude to their local LGM

572 position. Generally, two main glacial stages, LGM and post LGM (~17–16 ka), were observed within MIS 2 in

573 Mongolia (Rother et al., 2014; Batbaatar and Gillespie, 2016; Smith et al., 2016; Pötsch, 2017; Batbaatar et al., 2018).

574 Previous studies using granulometric, palynological, ostracod, and geochemical proxies from the Gobi Lakes

575 Valley reveal occurrence of cold and dry climates during the local LGM (19–18 ka) and Younger Dryas (Felauer et

576 al., 2012; Lee et al., 2013; Yu et al., 2017; Lehmkuhl et al., 2018; Yu et al., 2019; Mischke et al., 2020; Fig. 9). These

577 results are consistent with our exposure ages from two valleys. The warming trend was also present in the Gobi Lakes

578 Valley, where lakes once were desiccated during local LGM, and experienced water level increase after local LGM

579 (e.g., Yu et al., 2017; Mischke et al., 2020).

580

581

5.3. Aspect effect on the asynchronous glacial dynamic in Ikh Bogd

583 Our age dating result reveals that abrupt deglaciation occurred since ~20 ka in the Ikh Artsan glacier.

584 Exposure ages from the M_{J1} moraine (17 ka) should represent one of the following: glacier culmination, survival, or

585 temporary glacial stagnation of the LGM glacier, or glacier re-advance (Fig. 10). In either case, the culmination of the

586 Jargalant glacier near 17 ka implies a major difference in glacier mass balance between south- and north-facing

587 glaciers. Changes in glacier mass balance in small massif or mountain (intra-range) could show large spatial variation

588 due to local topography-induced factors, such as i) snow avalanching, ii) preferential deposition of wind-drifted snow

589 (Florentine et al., 2020), iii) solar radiation and iv) temperature.

590  i.  Periodically occurring snow avalanches support glacial accumulation. Most avalanches have steep
591     slopes between 25° and 50° to slide down (Luckman, 1977). Ikh Artsan and Jargalant valleys are
592     connected to the flat summit plateau and are less steep than the threshold slope of 25°. The average slope
593     was measured as 23° for Jargalant and 18.2° for Ikh Artsan. Very wet snow lubricated with water can
594     cause an avalanche on a slope of only 10 to 25° (Luckman, 1977). However, it is not significantly
595     relevant to our study area because Ikh Bogd and its neighboring area experienced very cold and
596     conditions during MIS 2 (e.g., Yu et al., 2019).

597  ii.  Wind-drifted snow accumulation occurs either with or without snowfall. Wind deflates the snow from
598     the windward slope and redistributes it into the leeward slope. However, the prevailing wind direction
599     of the study area is northwest to southeast, which is almost perpendicular to the orientations of the two
600     valleys. We assume the wind direction during MIS 2 was similar to the present with much strength.
601     Therefore, wind-drifted snow may not significantly affect glacier accumulation. For that reason, we used
602     the same precipitation value in both valleys.

603  iii.  North-facing slopes in the northern hemisphere receive less solar radiation because of the aspect effect.
604     Ikh Bogd locates in a mid-latitude great sunlight climate; furthermore, it has steeper relief which can
605     enhance the aspect effect. (Evans and Cox, 2005). Topographic shading can also influence glacier
606     response and mass balance in mountainous areas (Olson and Rupper, 2019). As expected, our modelling
607     results demonstrate that the north-facing slope receives less summer insolation than the south-facing
608     slope, resulting in reduced glacial melt (5-10%) under the same temperature conditions.

609  iv.  The vegetation, discontinuous permafrost, and modern and paleoglacier distribution and their magnitude
610     in semi-arid mid-latitude regions have contrasting temperatures and soil moisture on sunny and shady
611     slopes (Evans 2006; Barr and Spagnolo, 2015; Klinge et al., 2021). As a result of topographically induced
612     differences of solar radiation and evapotranspiration, forests (consisting of Siberian larch) and
613     discontinuous permafrost are limited to north-facing slopes, whereas mountain steppe covers south-
614     facing slopes in Mongolian forest-step zone (Klinge et al., 2021; Fig. 8b, c). Klinge et al. (2021)
615     determined that the annual incoming solar radiation, permafrost table depth, and soil moisture
616     (topographic wetness index) are significantly correlated. Aspect-driven solar radiation and temperature
617     contrast also give more glacier, lower (altitude) glacier, and larger glacier on the poleward slope (e.g.,
618     Evans 2006; Barr and Spagnolo, 2015). For instance, Sutai mountain (closest modern glacier to Ikh Bogd)
619     has large, well-developed valley glaciers that flow northward into low altitude from the ice dome. Still,
620     the glaciers at the south-facing slope end near the summit margin without developing into valley glaciers
621     (Fig. 8c). According to these facts, a small temperature difference is likely to be real and needs to be
622     considered. Our temperature index melt model revealed that applying lower temperature to the north-
623     facing glacier than to the south-facing glacier results in a large melt difference between the two valleys

624

625  Among the four topography-aspect induced factors, two are applicable on our study area; incoming solar radiation
626 and temperature difference in south- and north-facing slopes. Our temperature index melt model suggests that an

627 aspect-driven insolation change affects the amount of melt, however in a very small amount. This small reduction in

628 the melt due to the shading effect could not cause a significant difference in glacial mass balance or long-term glacier

629 stagnation or advance. Under the same temperature and different insolation, glaciers on the south- and north-facing

630 slopes across small regions behave almost synchronously. Both Ikh Artsan and Jargalant glaciers culminated near 20.2

631 ka and abruptly retreated to the cirque headwall. Also, their changes in glacial dynamic were almost the same (See

632 supplementary 2 file). However, no glacier stagnation was observed in the Jargalant valley around 17 ka (i.e., this

633 result does not match our exposure age dating). We sampled from possible most distal moraine from Jargalant valley

634 to avoid sampling from reworked boulders in the steep slope. Likewise, we could not find any other evidence that the

635 Jargalant glacier reached the trunk valley of the Bituut river. If we consider both glaciers moved synchronously, the

636 most distal moraine must locate more downvalley from the ~17 ka culmination. In this case, the geological evidence

637 (terminal moraine) near 20 ka must have been degraded by Bituut mainstream or/and reworked with the mass

638 movement.

639   When we set the site temperature of Jargalant slightly colder (-0.1 to -1 ℃) than in the Ikh Artsan, glaciers started

640 to behave differently, i.e., they retreat from their distal location asynchronously. When we apply 0.5 ℃ colder

641 temperature to Jargalant than Ikh Artsan, 2D ice surface modelling results are consistent with age dating results. The

642 Ikh Artsan glacier abruptly retreated from its maximum extent near 20.2 ka (age dating result was 20.1 ka). In contrast,

643 the Jargalant glacier advanced almost continuously until 17.8 ka and then began to retreat from its maximum extent

644 by 17.1 ka (age dating result was 17.2 ka) with a brief stagnation around its maximum extent. This result suggests that

645 the exposure age of ~17 ka corresponds to the most extensive glaciation in Jargalant valley. We also assume that the

646 exposure age (17.2 ± 1.5 ka) of the distal moraine (M_{J1}) is the age for maximum extent for the Jargalant valley (Figs.

647 6b and 6c) because this moraine was not like the small ridge left as a glacier stagnates during its retreat. The M_{J1}

648 moraine was larger than the other moraine sequences, large enough to mark the maximum advance of the glacier.

649   Based on the age dating and 2D ice surface modelling, we propose that the glaciers on the north- and south-

650 facing slopes of Ikh Bogd may have behaved asynchronously. Glacier volume and area changes are likely to be

651 sensitive to temperature changes in semi-arid and arid regions, such as Ikh Bogd. The glaciers of Ikh Artsan and

652 Jargalant behaved asynchronously due to aspect-induced temperature differences rather than differences in solar

653 insolation.

654

655

656 **5.4. Morphostratigraphic mismatch in exposure age dating from erratic boulders, Jargalant valley**

657 **5.4.1. Inheritance from the summit plateau**

658   The massif has a steep slope; in particular, the slope reaches 32–70° along cirque walls and incised valleys.

659 Colluvial materials covering hillslopes and long boulder corridors were mainly the results of the active mass wasting

660 process. Particularly, rockfall deposits forming scree and talus apron must be the product of steep slope failure of the

661 summit plateau (Fig. 11). We expected that inner moraine crests would present Holocene or HS-1 exposure in light of

662 morphostratigraphy. M_{J2}, M_{J3}, and M_{J4} moraine crests have exposure ages ranging from 636.2 to 35.9 ka (Table 4, Fig.

663 6). According to moraine stratigraphy, exposure ages of inner moraines cannot be older than the age of the distal

664   moraine. The apparent ages show antiquity and scatter in its distribution, which cannot be a single geologic event;

665   associating the mean age with the specific timing of glacial termination is not appropriate (Heyman et al., 2011b). It

666   was more likely that the exposure ages from M_{J2}, M_{J3}, and M_{J4} moraines were due to the inherited ^{10}Be concentration

667   produced during prior exposure in the boulders recycled from the cirque wall or paleo summit plateau by rockfall or

668   toppling during glaciation and/or paraglacial period. During termination of the farthest moraine, glacier was long

669   enough to pluck the fresh rocks out along its bed. Also, thick glacier would not allow inherited rocks fall onto the

670   glacier ice (Fig. 12d). After glacier retreat to the cirque, glacier thinning allowed rockfalls with inheritance to the ice

671   surface. Increase of inherited boulders would be contributed by enhanced rock-slope failure (de-buttressing) right after

672   rapid deglaciation (Cossart et al., 2008 ; Ballantyne and Stone, 2012; Hashemi et al., 2022) and ice segregation along

673   the bergschrund. Boulders with inheritance transported to the glacier toe as supraglacier debris. Plucking out by the

674   shortened glacier was not efficient to supply fresh rocks relative to the rock supply with summit plateau inheritance

675   (Fig. 12e).

676

677

678   **5.4.2. Cenozoic evolution of the low-lying, high-elevated summit plateau**

679   The flat summit plateau of the Ikh Bogd massif is considered an uplifted paleo-peneplanation surface. The

680   basement structure of Ikh Bogd was formed by the collision of the WNW-ESE to ENE-WSW oriented amalgamated

681   terranes throughout the Precambrian and Paleozoic (Şengör et al., 1993). ^{40}Ar/^{39}Ar ages from extrusive volcanic on

682   the Ikh Bogd summit and apatite fission-track data show two significant uplifts that occurred in the Gobi-Altai range

683   and Ikh Bogd history (Jolivet et al., 2007; Vassallo et al., 2007). The first uplift related to early to mid-Jurassic, the

684   region experienced crustal shortening events greater than 2 km. Gobi-Altai has been observed elsewhere in central

685   Asia through this event that is possibly due to a collision between Mongol-Okhotsk and Siberia or the Lhasa and

686   Qiangtang block to the far south in Tibet (Traynor and Sladen, 1995; Dewey et al., 1988; Cunningham, 2010). The

687   present erosional surface of the summit plateau formed just after this Jurassic exhumation and was preserved under a

688   negligible erosion rate. Preservation of this flat summit plateau and its fission-track age indicate quiescence without

689   significant vertical crustal motions continued until the last uplift began (Jolivet et al., 2007; Vassallo et al., 2007;

690   Cunningham, 2010).

691   The Gobi-Altai range is one of the northernmost far-fields affected by the Cenozoic tectonic collision of India

692   into Asia, which initiated the late Cenozoic reactivation and present-day stress regime (Cunningham et al., 1996;

693   Vassallo et al., 2007). According to the apatite fission track data of Vassallo et al. (2007), the onset of the last and

694   ongoing uplift corresponds to the late Cenozoic, 5 ± 3 Ma. This tectonic reactivation is responsible for creating the

695   high topography (~4000 m a.s.l) seen today, in the response to which faster exhumation is initiated as well (Vassallo

696   et al., 2007).

697   The paleo-erosion surfaces at high altitudes experienced rapid uplift after a long time of quiescence with low

698   erosion. Cosmogenic nuclides-based denudation rates from global paleo-erosion surfaces in diverse climatic, tectonic,

699   and lithologic environments do not exceed ~20 m Myr^{-1} (Byun et al., 2015). We obtained erosion rate for flat summit

700   plateau using production rate at summit plateau and ^{10}Be concentrations of reworked boulders from M_{J4}, M_{J3}, and M_{J2}

701   moraines. Calculated bedrock erosion rate for last ~600 ka for summit plateau ranged from 1.23 ± 0.10 mm kyr[-1] to

702   25.8 ± 5.75 m Myr[-1]. The erosion rate of 25.8 ± 5.75 m Myr[-1] was thought to be a maximum value because erosion

703   probably increases with the increasing elevation of the uplifting massif. This result was harmonious with the long-

704   term (since the last uplift) exhumation rate of 23.6 ± 3 m Ma[-1] (Vassallo et al., 2011) and Holocene erosion rate of 28

705   m Myr[-1] (Jolivet et al., 2007) for the massif. Whereas flatness and the lowest erosion rate of 1.23 ± 0.10 mm Myr[-1]

706   reveal negligible erosion and notable preservation of paleo-surface for several hundred thousand years. If this erosion

707   rate reflects an average rate that can be applied to the entire flat surface and has been maintained for the total uplift

708   period of the massif (Vassallo et al., 2007), it would account for only the 2 to 7.6 m of erosion.

709 **6. CONCLUSIONS**

710 Central Asian valley glaciers, including Ikh Bogd massif, expanded and shrank, presenting more complex behavior

711 relative to large ice sheets in the northern hemisphere. Regional climate and local non-climatic factors have been

712 playing an essential role in this complexity. Our [10]Be dating documents that glacier culmination in Ikh Artsan valley

713 on the southern slope occurred at 20.1 ka (M_{IA1}), generally falling within the gLGM, whereas large terminal moraine

714 formed around 17.2 ka (M_{J1}) in the Jargalant valley on the northern slope.

715 Asynchrony in glacier expansion has been reported from some of areas in the globe but has not been clearly

716 studied with a combination of geochronologic and numerical modeling approaches. Due to aspect-driven solar

717 insolation change, paleoglacier in the north-facing Jargalant valley melted slower (5-10%) than the glacier in Ikh

718 Artsan valley. However, this amount of melt difference could not produce glacier advance or stagnation for a long

719 period. Asynchronous glaciation was observed across the study area if the LGM summer temperature in Jargalant

720 valley was considered colder than Ikh Artsan and age dating result and modelling result were consistent when we

721 apply 0.5 °C lower temperature to Jargalant to than in Ikh Artsan. According to the lower temperature case, Jargalant

722 glacier retreated from the most extensive position 3000 years later than Ikh Artsan glacier. In the other words, our

723 modelling reveals that the temperature difference driven by aspect on both slopes significantly affects the glaciers to

724 survive longer than when the aspect-driven insolation only affects the glacier melt.

725 The glacial retreat began soon after the peak of local glacial maximum on both valleys and left several

726 sequences of inner moraines in their heads (cirques). Inner moraine at the south-facing cirque dated to ~ 13.5 ka

727 (Batbaatar et al., 2018), however on the north-facing cirque, transported boulders show a significantly old exposure

728 age (636.2 to 35.9 ka) for inner moraines (M_{J2} - M_{J4}). The summit plateau of the Ikh Bogd massif is one of the oldest

729 known tectonically uplifted surfaces on Earth. It is more likely that extremely old exposure ages are the result of

730 inheritance recycled from rock falls from the paleo-erosional surface of the summit plateau.

731 *Data availability.* The data that supports the findings of this study are available within the article [and its
732 supplementary material]
733

734 *Author contributions.* YBS planned the study and proceeded a field investigation with JSO, PK, KS, and CHL. YBS
735 designed a funding acquisition. JSO designed ^{10}Be lab experiments with RHH and BYY. CHL and MKS developed
736 a matlab code of the 2D ice surface modelling and performed the simulation. PK and YBS prepared the manuscript
737 with contributions from all co-authors.

738

739 *Competing interests.* The contact author has declared that neither they nor their co-authors have any competing
740 interests.

741

742 *Disclaimer.* Publisher's note: Copernicus Publications remains neutral with regard to jurisdictional claims in
743 published maps and institutional affiliations.

744

745 *Acknowledgments.* This work was supported by the Ministry of Education of the Republic of Korea and the National
746 Research Foundation of Korea (NRF-2018S1A5A2A01031348 for Y.B.S). We thank Dr. Dash for his sincere and
747 productive comments on the earlier version of the manuscript.

748

REFERENCES

©JAXA/METI., 2007. ALOS PALSAR L1.0 High-resolution terrain corrected dataset. Accessed through ASF DAAC, https://asf.alaska.edu, 25 June 2009. https://doi.org/10.5067/J4JVCFDDPEW1

ALAMGCM.: Topographic map of Mongolia, Geodesy and Cartography division of Agency for Land Administration and Management, Geodesy and Cartography of Mongolia, Ulaanbaatar, Mongolia, 1970.

An, Z., Kukla, G., Porter, S.C., Xiao, J.: Late Quaternary dust flow on the Chinese loess plateau, Catena, 18(2), 125-132, https://doi.org/10.1016/0341-8162(91)90012-M, 1991.

Balco, G: Contributions and unrealized potential contributions of cosmogenic nuclide exposure dating to glacier chronology, 1990–2010. Quat. Sci. Rev. 30, 3–27. https://doi.org/10.1016/j.quascirev.2010.11.003, 2011

Balco, G., Stone, J.O., Lifton, N.A., Dunai, T.J.: A complete and easily accessible means of calculating surface exposure ages or erosion rates from ^{10}Be and ^{26}Al measurements, Quat. Geochronol., 3(3), 174-195, https://doi.org/10.1016/j.quageo.2007.12.001, 2008.

Ballantyne, C.K., Stone, J.O.: Timing and periodicity of paraglacial rock-slope failures in the Scottish Highlands, Geomorphology, 186, 150-161, https://doi.org/10.1016/j.geomorph.2012.12.030, 2013.

Barr, I.D., Lovell, H.: A review of topographic controls on moraine distribution, Geomorphology, 226, 44-64, https://doi.org/10.1016/j.geomorph.2014.07.030, 2014.

Barr, I. D., & Spagnolo, M.: Glacial cirques as palaeoenvironmental indicators: Their potential and limitations. Earth-Sci. Rev, 151, 48-78, https://doi.org/10.1016/j.earscirev.2015.10.004, 2015

Batbaatar, J.: Quaternary Glaciation in Central Asia (Doctoral dissertation), 2018.

Batbaatar, J., Gillespie, A.R.: Outburst floods of the Maly Yenisei. Part II–new age constraints from Darhad basin, Int. Geol. Rev., 58(14), 1753-1779, https://doi.org/10.1080/00206814.2016.1193452, 2016.

Batbaatar, J., Gillespie, A.R., Fink, D., Matmon, A., Fujioka, T.: Asynchronous glaciations in arid continental climate, Quat. Sci. Rev., 182, 1-19, https://doi.org/10.1016/j.quascirev.2017.12.001, 2018.

Bayasgalan, A., Jackson, J., Ritz, J.F., Carretier, S.J.T.: Field examples of strike-slip fault terminations in Mongolia and their tectonic significance. Tectonics, 18(3), 394-411, https://doi.org/10.1029/1999TC900007, 1999.

Benn, D. I., Hulton, N. R.: An ExcelTM spreadsheet program for reconstructing the surface profile of former mountain glaciers and ice caps, Comput. Geosci, v. 36, no. 5, p. 605-610, https://doi.org/10.1016/j.cageo.2009.09.016, 2010,

Benn, D.I., Lehmkuhl, F.: Mass balance and equilibrium-line altitudes of glaciers in high-mountain environments, Quat. Int., 65(Supplement C), 15-29, https://doi.org/10.1016/S1040-6182(99)00034-8, 2000.

Berger, A., Loutre, M.-F.: Insolation values for the climate of the last 10 million years, Quat. Sci. Rev, v. 10, no. 4, p. 297-317, https://doi.org/10.1016/0277-3791(91)90033-Q, 1991,

Berkey, C.P., Morris, F.K.: The peneplanes of Mongolia, Am. Mus. Novit., 136, 1-11, 1924.

Blomdin, R., Stroeven, A.P., Harbor, J.M., Gribenski, N., Caffee, M.W., Heyman, J., Rogozhina, I., Ivanov, M.N., Petrakov, D.A., Walther, M.: Timing and dynamics of glaciation in the Ikh Turgen Mountains, Altai region, High Asia, Quat. Geochronol., 47, 54-71, https://doi.org/10.1016/j.quageo.2018.05.008, 2018.

Blomdin, R., Stroeven, A.P., Harbor, J.M., Lifton, N.A., Heyman, J., Gribenski, N., Petrakov, D.A., Caffee, M.W., Ivanov, M.N., Hättestrand, C., Rogozhina, I., Usubaliev, R.: Evaluating the timing of former glacier expansions in the Tian Shan: A key step towards robust spatial correlations, Quat. Sci. Rev., 153, 78-96, https://doi.org/10.1016/j.quascirev.2016.07.029, 2016.

Buizert, C., Keisling, B., Box, J., He, F., Carlson, A., Sinclair, G., and DeConto, R.: Greenland-wide seasonal temperatures during the last deglaciation, Geophys. Res. Lett., v. 45, no. 4, p. 1905-1914, https://doi.org/10.1002/2017GL075601, 2018.

Byun, J., Heimsath, A.M., Seong, Y.B., Lee, S.Y.: Erosion of a high-altitude, low-relief area on the Korean Peninsula: implications for its development processes and evolution, Earth Surf. Process. Landf., 40(13), 1730-1745, https://doi.org/10.1002/esp.3749, 2015.

Chai, L. T., Wong, C. J., James, D., Loh, H. Y., Liew, J. J. F., Wong, W. V. C., & Phua, M. H.: Vertical accuracy comparison of multi-source Digital Elevation Model (DEM) with Airborne Light Detection and Ranging (LiDAR). In IOP Conference Series: Earth. Environ. Sci., 1053, No. 1, p. 012025, IOP Publishing, 10.1088/1755-1315/1053/1/012025, 2022.

Chauvenet, W.: A Manual of spherical and practical astronomy-Vol. 1: Spherical astronomy; Vol. 2: Theory and use of astronomical instruments. Method of least squares, 5th ed., revised and corr, Dover Publication, New York, 1960

Chen, Y., Li, Y., Wang, Y., Zhang, M., Cui, Z., Yi, C., Liu, G.: Late Quaternary glacial history of the Karlik Range, easternmost Tian Shan, derived from [10]Be surface exposure and optically stimulated luminescence datings, Quat. Sci. Rev., 115, 17-27, https://doi.org/10.1016/j.quascirev.2015.02.010, 2015.

Ciner, A., Sarikaya, M. A., Yildirim, C.: Misleading old age on a young landform? The dilemma of cosmogenic inheritance in surface exposure dating: Moraines vs. rock glaciers, Quat. Geochronol., 42, 76-88, https://doi.org/10.1016/j.quageo.2017.07.003, 2017.

Clark, P.U., Dyke, A.S., Shakun, J.D., Carlson, A.E., Clark, J., Wohlfarth, B., Mitrovica, J.X., Hostetler, S.W., McCabe, A.M.: The last glacial maximum, Science, 325(5941), 710-714, https://doi.org/10.1126/science.1172873, 2009.

Cossart, E., Braucher, R., Fort, M., Bourlès, D., Carcaillet, J.: Slope instability in relation to glacial debuttressing in alpine areas (Upper Durance catchment, southeastern France): evidence from field data and 10Be cosmic ray exposure ages, Geomorphology, 95(1-2), 3-26, https://doi.org/10.1016/j.geomorph.2006.12.022, 2008.

Cunningham, D.: Tectonic setting and structural evolution of the Late Cenozoic Gobi-Altai orogen, J. Geol. Soc. London., 338(1), 361-387, https://doi.org/10.1144/SP338.17, 2010.

Cunningham, W.D., Windley, B.F., Dorjnamjaa, D., Badamgarov, J., Saandar, M.: Late Cenozoic transpression in southwestern Mongolia and the Gobi-Altai-Tien Shan connection, Earth Planet. Sci. Lett., 140(1-4), 67-81, https://doi.org/10.1016/0012-821X(96)00048-9, 1996.

Dahl, S. O., Bakke, J., Lie, Ø., & Nesje, A.: Reconstruction of former glacier equilibrium-line altitudes based on proglacial sites: an evaluation of approaches and selection of sites. Quat. Sci. Rev., 22(2-4), 275-287, https://doi.org/10.1016/S0277-3791(02)00135-X, 2003

823 Delmas, M., Calvet, M., Gunnell, Y., Braucher, R., & Bourlès, D.: Palaeogeography and 10Be exposure-age
824   chronology of Middle and Late Pleistocene glacier systems in the northern Pyrenees: implications for
825   reconstructing regional palaeoclimates, Palaeogeo. Palaeoclimatol. Palaeoecol., 305(1-4), 109-122,
826   https://doi.org/10.1016/j.palaeo.2011.02.025, 2011.

827 Delmas, M., Gunnell, Y., Braucher, R., Calvet, M., & Bourlès, D.: Exposure age chronology of the last glaciation in
828   the eastern Pyrenees, Quat. Res., 69(2), 231-241, https://doi.org/10.1016/j.yqres.2007.11.004, 2008.

829 Devyatkin, E.: Structures and formational complexes of the Cenozoic activated stage. Tectonics of the Mongolian
830   People's Republic, Nauka, 41, 182-195, 1974.

831 Dewey, J.F., Shackleton, R.M., Chengfa, C., Yiyin, S.: The tectonic evolution of the Tibetan Plateau, Philos. Trans.
832   Royal Soc. A., 327(1594), 379-413, https://doi.org/10.1098/rsta.1988.0135, 1988.

833 EIC.: Geologic map of Mongolia 1:1000000. Environment Information Center of National Agency for Meteorology,
834   Hydrology and Environmental Monitoring, Ulaanbaatar, Mongolia, 1981.

835 Evans, I. S.: Local aspect asymmetry of mountain glaciation: a global survey of consistency of favoured directions for
836   glacier numbers and altitudes. Geomorphology, 73(1-2), https://doi.org/10.1016/j.geomorph.2005.07.009
837   166-184, 2006

838 Evans, I.S., Cox, N.J.: Global variations of local asymmetry in glacier altitude: separation of north–south and east–
839   west components, J. Glaciol., 51(174), 469-482, https://doi.org/10.3189/172756505781829205, 2005.

840 Felauer, T., Schlütz, F., Murad, W., Mischke, S., Lehmkuhl, F.: Late Quaternary climate and landscape evolution in
841   arid Central Asia: A multiproxy study of lake archive Bayan Tohomin Nuur¢, Gobi desert, southern Mongolia,
842   J. Asian. Earth. Sci., 48, 125-135, https://doi.org/10.1016/j.jseaes.2011.12.002, 2012.

843 Ferreira, Z. A., & Cabral, P:. A Comparative study about vertical accuracy of four freely available digital elevation
844   models: a case study in the Balsas river watershed, Brazil. ISPRS Int. J. Geo-Inf., 11(2), 106,
845   https://doi.org/10.3390/ijgi11020106, 2022

846 Fletcher, W.J., Goni, M.F.S., Allen, J.R., Cheddadi, R., Combourieu-Nebout, N., Huntley, B., Lawson, I., Londeix,
847   L., Magri, D., Margari, V.: Millennial-scale variability during the last glacial in vegetation records from
848   Europe, Quat. Sci. Rev., 29(21-22), 2839-2864, https://doi.org/10.1016/j.quascirev.2009.11.015, 2010.

849 Florentine, C., Harper, J., Fagre, D.: Parsing complex terrain controls on mountain glacier response to climate forcing,
850   Glob. Planet. Change., 191, 103209, https://doi.org/10.1016/j.gloplacha.2020.103209, 2020.

851 Gillespie, A.R., Burke, R.M., Komatsu, G., Bayasgalan, A.: Late Pleistocene glaciers in Darhad basin, northern
852   Mongolia, Quat. Res., 69(2), 169-187, https://doi.org/10.1016/j.yqres.2008.01.001, 2008.

853 Goldthwait, R.P.: Mountain glaciers of the Presidential Range in New Hampshire, Arc. Alp. Res., 2(2), 85-102,
854   https://doi.org/10.1080/00040851.1970.12003566, 1970.

855 Gosse, J.C., Phillips, F.M.: Terrestrial in situ cosmogenic nuclides: theory and application, Quat. Sci. Rev., 20(14),
856   1475-1560, https://doi.org/10.1016/S0277-3791(00)00171-2, 2001.

857 Gribenski, N., Jansson, K. N., Preusser, F., Harbor, J. M., Stroeven, A. P., Trauerstein, M., ... & Zhang, W.: Re-
858   evaluation of MIS 3 glaciation using cosmogenic radionuclide and single grain luminescence ages, Kanas
859   Valley, Chinese Altai. J. Quat. Sci., 33(1), 55-67, https: //doi.org/10.1002/jqs.2998, 2018

860 Hashemi, K., Sarıkaya, M.A., Görüm, T., Wilcken, K.M., Çiner, A., Žebre, M., Stepišnik, U., Yıldırım, C.: The
861   Namaras rock avalanche: Evidence of mid-to-late Holocene paraglacial activity in the Central Taurus
862   Mountains, SW Turkey, Geomorphology, 408, 108261, https://doi.org/10.1016/j.geomorph.2022.108261,
863   2022.

864 Heyman, J.: Paleoglaciation of the Tibetan Plateau and surrounding mountains based on exposure ages and ELA
865   depression estimates, Quat. Sci. Rev., 91, 30-41, https://doi.org/10.1016/j.quascirev.2014.03.018, 2014.

866 Heyman, J., Stroeven, A.P., Caffee, M.W., Hättestrand, C., Harbor, J.M., Li, Y., Alexanderson, H., Zhou, L., Hubbard,
867   A.: Palaeoglaciology of Bayan Har Shan, NE Tibetan Plateau: exposure ages reveal a missing LGM
868   expansion, Quat. Sci. Rev., 30(15-16), 1988-2001, https://doi.org/10.1016/j.quascirev.2011.05.002, 2011a.

869 Heyman, J., Stroeven, A.P., Harbor, J.M., Caffee, M.W.: Too young or too old: evaluating cosmogenic exposure
870   dating based on an analysis of compiled boulder exposure ages, Earth Planet. Sci. Lett., 302(1-2), 71-80,
871   https://doi.org/10.1016/j.epsl.2010.11.040, 2011b.

872 Hock, R.: Modelling of glacier melt and discharge: ETH Zurich-, 1999, A distributed temperature-index ice-and
873   snowmelt model including potential direct solar radiation, J. Glaciol., v. 45, no. 149, p. 101-111,
874   https://doi.org/10.3189/S0022143000003087, 1998,

875 Hock, R.: A distributed temperature-index ice-and snowmelt model including potential direct solar radiation, J.
876   Glaciol., 45(149), 101-111, https://doi.org/10.3189/S0022143000003087, 1999.

877 Hughes, P.D., Gibbard, P.L., Ehlers, J.: Timing of glaciation during the last glacial cycle: evaluating the concept of a
878   global 'Last Glacial Maximum'(LGM). Earth-Sci. Rev., 125, 171-198,
879   https://doi.org/10.1016/j.earscirev.2013.07.003, 2013.

880 Iqbal, M.: An Introduction to Solar Radiation, New York, Academic Press, 1983

881 Jiménez-Sánchez, M., Rodríguez-Rodríguez, L., García-Ruiz, J.M., Domínguez-Cuesta, M.J., Farias, P., Valero-
882   Garcés, B.L., Moreno, A., Valcárcel, M.: A review of glacial geomorphology and chronology in northern
883   Spain: timing and regional variability during the last glacial cycle. Geomorphology 196, 50–64,
884   https://doi.org/10.1016/j.geomorph.2012.06.009, 2013

885 Jolivet, M., Ritz, J.-F., Vassallo, R., Larroque, C., Braucher, R., Todbileg, M., Chauvet, A., Sue, C., Arnaud, N., De
886   Vicente, R.: Mongolian summits: an uplifted, flat, old but still preserved erosion surface, Geology, 35(10),
887   871-874, https://doi.org/10.1130/G23758A.1, 2007.

888 Jones, R., Small, D., Cahill, N., Bentley, M., Whitehouse, P.: iceTEA: tools for plotting and analysing cosmogenic-
889   nuclide surface-exposure data from former ice margins, Quat. Geochronol., 51, 72-86,
890   https://doi.org/10.1016/j.quageo.2019.01.001, 2019.

891 Jouzel, J., Stievenard, M., Johnsen, S.J., Landais, A., Masson-Delmotte, V., Sveinbjornsdottir, A., Vimeux, F., Von
892   Grafenstein, U., White, J.W.: The GRIP deuterium-excess record, Quat. Sci. Rev., 26(1-2), 1-17,
893   https://doi.org/10.1016/j.quascirev.2006.07.015, 2007.

894 Karger, D.N., Conrad, O., Böhner, J., Kawohl, T., Kreft, H., Soria-Auza, R.W., Zimmermann, N.E., Linder, H.P.,
895   Kessler, M.: Climatologies at high resolution for the earth's land surface areas. Sci. Data., 4, 170122,
896   https://doi.org/10.1038/sdata.2017.122, 2017.

897   Khandsuren, P., Seong, Y.B., Oh, J.S., Rhee, H.H., Sandag, K., Yu, B.Y.: Late Quaternary glacial history of Khentey
898   Mountains, Central Mongolia, Boreas, 48(3), 779-799, doi.org/10.1111/bor.12386, 2019.

899   Kirkbride, M., Winkler, S.: Correlation of Late Quaternary moraines: impact of climate variability, glacier response,
900   and chronological resolution, Quat. Sci. Rev., 46, 1-29, https://doi.org/10.1016/j.quascirev.2012.04.002,
901   2012.

902   Klinge, M., Schneider, F., Dulamsuren, C., Arndt, K., Bayarsaikhan, U., & Sauer, D.: Interrelations between relief,
903   vegetation, disturbances, and permafrost in the forest-steppe of central Mongolia. Earth Surf. Process.
904   Landf., 46(9), 1766-1782, https://doi.org/10.1002/esp.5116, 2021

905   Kohl, C.P., Nishiizumi, K.: Chemical isolation of quartz for measurement of in situ -produced cosmogenic nuclides,
906   Geochim. Cosmochim. Acta, 56(9), 3583-3587, https://doi.org/10.1016/0016-7037(92)90401-4, 1992.

907   Koppes, M., Gillespie, A.R., Burke, R.M., Thompson, S.C., Stone, J.: Late quaternary glaciation in the Kyrgyz Tien
908   Shan. Quat. Sci. Rev., 27(7-8), 846-866, https://doi.org/10.1016/j.quascirev.2008.01.009, 2008.

909   Laabs, B. J., Licciardi, J. M., Leonard, E. M., Munroe, J. S., & Marchetti, D. W.: Updated cosmogenic chronologies
910   of Pleistocene mountain glaciation in the western United States and associated paleoclimate inferences, Quat.
911   Sci. Rev., 242, 106427, https://doi.org/10.1016/j.quascirev.2020.106427, 2020.

912   Laabs, B. J. C., & Munroe, J. S.: Late Pleistocene mountain glaciation in the Lake Bonneville basin, In Developments
913   in Earth. Surf. Process., Vol. 20, pp. 462-503, https://doi.org/10.1016/B978-0-444-63590-7.00017-2, 2016

914   Laabs, B. J., Marchetti, D. W., Munroe, J. S., Refsnider, K. A., Gosse, J. C., Lips, E. W., ... & Singer, B. S.; Chronology
915   of latest Pleistocene mountain glaciation in the western Wasatch Mountains, Utah, USA. Quaternary
916   Research, 76(2), 272-284, https://doi.org/10.1016/j.yqres.2011.06.016, 2011

917   Laabs, B. J., Refsnider, K. A., Munroe, J. S., Mickelson, D. M., Applegate, P. J., Singer, B. S., & Caffee, M. W.:
918   Latest Pleistocene glacial chronology of the Uinta Mountains: support for moisture-driven asynchrony of the
919   last deglaciation, Quat. Sci. Rev., 28(13-14), 1171-1187, https://doi:10.1016/j.quascirev.2008.12.012, 2009.

920   Lee, M.K., Lee, Y.I., Lim, H.S., Lee, J.I., Yoon, H.I.: Late Pleistocene–Holocene records from Lake Ulaan, southern
921   Mongolia: implications for east Asian palaeomonsoonal climate changes, J. Quat. Sci., 28(4), 370-378,
922   https://doi.org/10.1002/jqs.2626, 2013.

923   Lehmkuhl, F., Grunert, J., Hülle, D., Batkhishig, O., Stauch, G.: Paleolakes in the Gobi region of southern Mongolia,
924   Quat. Sci. Rev., 179, 1-23, https://doi.org/10.1016/j.quascirev.2017.10.035, 2018.

925   Li, Y., Liu, G., Chen, Y., Li, Y., Harbor, J., Stroeven, A.P., Caffee, M., Zhang, M., Li, C., Cui, Z.: Timing and extent
926   of Quaternary glaciations in the Tianger Range, eastern Tian Shan, China, investigated using [10]Be surface
927   exposure dating, Quat. Sci. Rev., 98, 7-23, https://doi.org/10.1016/j.quascirev.2014.05.009, 2014.

928   Licciardi, J. M., Clark, P. U., Brook, E. J., Elmore, D., & Sharma, P.: Variable responses of western US glaciers during
929   the last deglaciation, Geology, 32(1), 81-84, https://doi.org/10.1130/G19868.1, 2004

930   Licciardi, J. M., Clark, P. U., Brook, E. J., Pierce, K. L., Kurz, M. D., Elmore, D., & Sharma, P.: Cosmogenic 3He
931   and 10Be chronologies of the late Pinedale northern Yellowstone ice cap, Montana, USA, Geology, 29(12),
932   1095-1098, https://doi.org/10.1130/0091-7613(2001)029<1095:CHABCO>2.0.CO;2, 2001.

933 Licciardi, J. M., & Pierce, K. L.: History and dynamics of the Greater Yellowstone Glacial System during the last two
934   glaciations, Quat. Sci. Rev., 200, 1-33, https://doi.org/10.1016/j.quascirev.2018.08.027, 2018

935 Lifton, N., Sato, T., Dunai, T.J.: Scaling in situ cosmogenic nuclide production rates using analytical approximations
936   to atmospheric cosmic-ray fluxes, Earth Planet, Sci. Lett., 386, 149-160,
937   https://doi.org/10.1016/j.epsl.2013.10.052, 2014.

938 Luckman, B. H.: The Geomorphic Activity of Snow Avalanches. Geografiska Annaler: Series A, Phys. Geogr.,
939   59(1-2), 31-48, https://doi.org/10.1080/04353676.1977.11879945, 1977.

940 Meierding, T. C.: Late Pleistocene glacial equilibrium-line altitudes in the Colorado Front Range: a comparison of
941   methods. Quat. Res., 18(3), 289-310. Research 18, 289-310, https://doi.org/10.1016/0033-5894(82)90076-X,
942   1982

943 Mischke, S., Lee, M.K., Lee, Y.I.: Climate history of southern Mongolia since 17 ka: The ostracod, gastropod and
944   charophyte record from Lake Ulaan, Front, Earth Sci., 8, 221, https://doi.org/10.3389/feart.2020.00221,
945   2020.

946 NAMHEM.: Climate data. Institute for Hydrology and Aviation Meteorological Center of National Agency for
947   Meteorology, Hydrology and Environmental Monitoring, Ulaanbaatar, Mongolia, 2020.

948 Nishiizumi, K., Imamura, M., Caffee, M., Southon, J., Finkel, R., McAninch, J.: Absolute calibration of [10]Be AMS
949   Standards, Nucl. Instrum. Methods Phys. Res. B., 258(2), 403-413,
950   https://doi.org/10.1016/j.nimb.2007.01.297, 2007.

951 National Oceanic and Atmospheric Administration.: US standard atmosphere (Vol. 76)., 1976

952 Oliva, M., Palacios, D., Fernández-Fernández, J. M., Rodríguez-Rodríguez, L., García-Ruiz, J. M., Andrés, N., ... &
953   Hughes, P. D.: Late Quaternary glacial phases in the Iberian Peninsula, Earth-Sci, Rev., 192, 564-600,
954   https://doi.org/10.1016/j.earscirev.2019.03.015, 2019.

955 Olson, M., & Rupper, S.: Impacts of topographic shading on direct solar radiation for valley glaciers in complex
956   topography, The Cryosphere, 13(1), 29-40, 2019.

957 Palacios, D., Stokes, C. R., Phillips, F. M., Clague, J. J., Alcalá-Reygosa, J., Andrés, N., ... & Ward, D. J.: The
958   deglaciation of the Americas during the Last Glacial Termination, Earth-Sci. Rev., 203, 103113,
959   https://doi.org/10.1016/j.earscirev.2020.103113, 2020.

960 Porter, S.C.: Snowline depression in the tropics during the Last Glaciation. Quat. Sci. Rev., 20(10), pp.1067-
961   1091, https://doi.org/10.1016/S0277-3791(00)00178-5, 2001

962 Pötsch, S.: Dynamics and paleo-climatic forcing of late Pleistocene glaciers in the Turgen and Khangai mountains
963   (Mongolia) reconstructed from geomorphology, [10]Be surface exposure dating, and ice flow modelling. Ph.D.
964   thesis, Greifswald, Finsterwalde, 2017.

965 Quirk, B. J., Moore, J. R., Laabs, B. J., Plummer, M. A., & Caffee, M. W.: Latest Pleistocene glacial and climate
966   history of the Wasatch Range, Utah, Quat. Sci. Rev., 238, 106313,
967   https://doi.org/10.1016/j.quascirev.2020.106313, 2020.

968 Ross, S.M.: Peirce's criterion for the elimination of suspect experimental data, J. Eng. Technol., 20(2), 38-41, 2003.

Rother, H., Lehmkuhl, F., Fink, D., Nottebaum, V.: Surface exposure dating reveals MIS-3 glacial maximum in the Khangai Mountains of Mongolia, Quat. Res., 82(2), 297-308, https://doi.org/10.1016/j.yqres.2014.04.006, 2014.

Sanders, J. W., Cuffey, K. M., Moore, J. R., MacGregor, K. R., & Kavanaugh, J. L.: Periglacial weathering and headwall erosion in cirque glacier bergschrunds. Geology, 40(9), 779-782, https://doi:10.1130/G33330.1, 2012

Şengör, A., Natal'In, B., Burtman, V.: Evolution of the Altaid tectonic collage and Palaeozoic crustal growth in Eurasia, Nature, 364(6435), 299-307, https://doi.org/10.1038/364299a0, 1993.

Seong, Y.B., Dorn, R.I., Yu, B.Y.: Evaluating the life expectancy of a desert pavement, Earth-Sci.Rev., 162, 129-154, https://doi.org/10.1016/j.earscirev.2016.08.005, 2016.

Shackleton, N.: Oxygen isotope analyses and Pleistocene temperatures re-assessed, Nature, 215(5096), 15-17, https://doi.org/10.1038/215015a0, 1967.

Shackleton, N.J.: The 100,000-year ice-age cycle identified and found to lag temperature, carbon dioxide, and orbital eccentricity, Science, 289(5486), 1897-1902, https://doi.org/10.1126/science.289.5486.1897, 2000.

Skinner, L., Shackleton, N.: An Atlantic lead over Pacific deep-water change across Termination I: implications for the application of the marine isotope stage stratigraphy, Quat. Sci. Rev., 24(5-6), 571-580, https://doi.org/10.1016/j.quascirev.2004.11.008, 2005.

Smith, S.G., Wegmann, K.W., Ancuta, L.D., Gosse, J.C., Hopkins, C.E.: Paleotopography and erosion rates in the central Hangay Dome, Mongolia: Landscape evolution since the mid-Miocene, J. Asian. Earth. Sci., 125, 37-57 DOI: https://doi.org/10.1016/j.jseaes.2016.05.013, 2016.

Tang, Z., & Fang, J.: Temperature variation along the northern and southern slopes of Mt. Taibai, China, Agric. For. Meteorol., 139(3-4), 200-207, https://doi.org/10.1016/j.agrformet.2006.07.001, 2006.

Tarasov, P., Peyron, O., Guiot, J., Brewer, S., Volkova, V., Bezusko, L., Dorofeyuk, N., Kvavadze, E., Osipova, I., and Panova, N.: Last Glacial Maximum climate of the former Soviet Union and Mongolia reconstructed from pollen and plant macrofossil data, Clim. Dyn., v. 15, no. 3, p. 227-240, https://doi.org/10.1007/s003820050278, 1999,

Thackray, G. D.: Varied climatic and topographic influences on Late Pleistocene mountain glaciation in the western United States, J. Quat. Sci.,: Published for the Quaternary Research Association, 23(6-7), 671-681, https://doi.org/10.1002/jqs.1210, 2008.

Thompson, W.G., Spiegelman, M.W., Goldstein, S.L., Speed, R.C.: An open-system model for U-series age determinations of fossil corals, Earth Planet. Sci. Lett., 210(1-2), 365-381, https://doi.org/10.1016/S0012-821X(03)00121-3, 2003.

Traynor, J., Sladen, C.: Tectonic and stratigraphic evolution of the Mongolian People's Republic and its influence on hydrocarbon geology and potential, Mar. Pet. Geol., 12(1), 35-52, https://doi.org/10.1016/0264-8172(95)90386-X, 1995.

1004   Vassallo, R., Jolivet, M., Ritz, J.-F., Braucher, R., Larroque, C., Sue, C., Todbileg, M., Javkhlanbold, D.: Uplift age
1005   and rates of the Gurvan Bogd system (Gobi-Altay) by apatite fission track analysis, Earth Planet. Sci. Lett.,
1006   259(3-4), 333-346, https://doi.org/10.1016/j.epsl.2007.04.047, 2007.

1007   Vassallo, R., Ritz, J.-F., Carretier, S.: Control of geomorphic processes on [10]Be concentrations in individual clasts:
1008   Complexity of the exposure history in Gobi-Altay range (Mongolia), Geomorphology, 135(1-2), 35-47,
1009   https://doi.org/10.1016/j.geomorph.2011.07.023, 2011.

1010   Wang, Y.-J., Cheng, H., Edwards, R.L., An, Z., Wu, J., Shen, C.-C., Dorale, J.A.: A high-resolution absolute-dated
1011   late Pleistocene monsoon record from Hulu Cave, China, Science, 294(5550), 2345-2348,
1012   https://doi.org/10.1126/science.1064618, 2001.

1013   Young, N. E., Briner, J. P., Leonard, E. M., Licciardi, J. M., & Lee, K.: Assessing climatic and nonclimatic forcing
1014   of Pinedale glaciation and deglaciation in the western United States, Geology, 39(2), 171-174,
1015   https://doi.org/10.1130/G31527.1, 2011.

1016   Yu, K., Lehmkuhl, F., Diekmann, B., Zeeden, C., Nottebaum, V., Stauch, G.: Geochemical imprints of coupled
1017   paleoenvironmental and provenance change in the lacustrine sequence of Orog Nuur, Gobi Desert of
1018   Mongolia, J. Paleolimnol., 58(4), 511-532, https://doi.org/10.1007/s10933-017-0007-7, 2017.

1019   Yu, K., Lehmkuhl, F., Schlütz, F., Diekmann, B., Mischke, S., Grunert, J., Murad, W., Nottebaum, V., Stauch, G.,
1020   Zeeden, C.: Late Quaternary environments in the Gobi Desert of Mongolia: Vegetation, hydrological, and
1021   palaeoclimate evolution, Palaeogeogr. Palaeoclimatol. Palaeoecol., 514, 77-91,
1022   https://doi.org956/10.1016/j.palaeo.2018.10.004, 2019.

1023   Zhang, S., Zhao, H., Sheng, Y., Chen, S., Li, G., & Chen, F.: Late Quaternary lake level record of Orog Nuur, southern
1024   Mongolia, revealed by optical dating of paleo-shorelines, Quat. Geochronol, 72, 101370,
1025   https://doi.org/10.1016/j.quageo.2022.101370, 2022.

1026

1027 **LIST OF TABLES**

1032

1033

1034 **LIST OF FIGURES**

1050   **Table 1.** Site parameters and glacier parameters used for the 2D ice surface model

Variable	Value	Unit
Time interval	22-16	ka
Day type	1 (calendar day)	
Day interval	152-243 (summer)	
Average elevation of site	3265.3	m
Modern summer temperature of Ikh Artsan	5.4	°C
Modern summer temperature of Jargalant	4.9	°C
LGM anomaly	-5.5	°C
Snow ratio (when temperature is below 0°C)	0.35	
Elevation of initial glacier's toe (Ikh Artsan)	3385.1	m
Elevation of initial glacier's toe (Jargalant)	3360.9	m
Elevation of the distal moraine (Ikh Artsan)	3222.2	m
Elevation of the distal moraine (Jargalant)	2997.2	m
Headwall altitude (Ikh Artsan)	3508.3	m
Headwall altitude (Jargalant)	3533.3	m
Glacial bed shear stress (Ikh Artsan)	100	kPa
Glacial bed shear stress (Jargalant)	200	kPa

1051

1052

1053   **Table 2.** Key parameters of glacial mass balance model

Variable		Optimized values/Unit	Variable		Optimized values/Unit
	Mass balance calculation (m, mm)			**Air pressure calculation (P_h, Pa)**	
c	Accumulation	mm, m	P_0	Pressure at reference point (sea level)	1013.25 Pa
a	Ablation/melt	mm, m	T_h	Air temperature at the height h	Pa
	Melt calculation (a, m)		T_0	Air temperature at the reference point	288.15 K
n	Number of time steps per day		M	Mass per air molecule	0.0290 kg mol^{-1}
MF	Melt factor	1.8 mm d^{-1} °C^{-1}	g	Acceleration due to gravity	9.8067 m s^{-2}
a_{ice}	Radiation coefficient for ice surfaces	0.0008	R	Universal gas constant	8.3143 mol K
I	Potential clear-sky direct solar radiation at the glacier	W m^{-2}	L	Atmospheric lapse rate	-0.008 K m^{-1}
T	Monthly air temperature	°C		**Zenith angle calculation (Z, °) and angle of incidence (θ, °)**	
	Insolation calculation (I, w m^{-2})		δ	Solar declination angle	°/Radian
I_0	Solar constant	1367 W m^{-2}	φ	Latitude	°/Radian
R_m/R	Eccentricity correction factor of the earth's orbit		ω	Hour angle	°/Radian
Ψ_a	Atmospheric transmissivity	0.75	β	Slope inclination angle	°/Radian
P_h	Air pressure at the height	Pa	γ	Surface azimuth angle	°/Radian
P_0	Air pressure at reference point (sea level)	1013.25 Pa			
Z	Zenith angle	°			
θ	Angle of incidence	°			

1054

1055   **Table 3.** LGM ELA reconstruction

Sites	Top of the rock cliff (m a.s.l)	Altitude of cirque floor (m a.s.l)	Headwall altitude [a] (m a.s.l)	Toe altitude, LGM (m a.s.l)	THAR ELA [b] (m a.s.l)
Jargalant valley	3620	3360	3533	2997	3308
Ikh Artsan valley	3560	3385	3508	3222	3388
Average					3348

1056   [a] Headwall altitude for LGM glaciers was selected at one-third of the altitude difference between the top of the rock
1057   cliff and the cirque floor (Goldthwait, 1970).

1058   [b] THAR of 0.58 was used for calculating LGM ELA (Batbaatar et al., 2018). ALOS PALSAR DEM with spatial
1059   resolution of 12.5 m is used to extract corresponding elevations. Altimetric error (vertical uncertainty) is ~5-7 m (Chai
1060   et al., 2022, Ferreira and Cabral, 2022).

Table 4. Result of ^{10}Be exposure age dating

Moraine group	Name	Latitude (°N, DD)	Longitude (°E, DD)	Elevation (m a.s.l)	Thickness[a] (cm)	Shielding factor[b]	Quartz[c] (g)	Be carrier[d] (g)	^{10}Be/^{9}Be[e,f] (10^{-13})	^{10}Be conc.[d,f] $(10^5$ atoms g$^{-1})$	Exposure age[f,g,i] (ka) LSDn
M_{IA1}	IAM001	44.95421	100.2602	3289	2	0.7746	20.3	0.3729	6.0 ± 0.2	7.7 ± 0.3	19.9 ± 1.4
	IAM002	44.95429	100.26022	3290	2.5	0.7746	17.52	0.3796	5.3 ± 0.2	8.0 ± 0.3	20.7 ± 1.4
	IAM003	44.95427	100.2603	3289	3.5	0.7746	20	0.3849	6.1 ± 0.2	8.1 ± 0.3	21.2 ± 1.5
	IAM004	44.95438	100.26035	3289	3.5	0.7746	14.69	0.3958	4.1 ± 0.1	7.6 ± 0.3	19.9 ± 1.4
	IAM005	44.95435	100.26015	3290	3	0.7746	19.75	0.3704	5.7 ± 0.2	7.4 ± 0.2	19.3 ± 1.3
	IAM006	44.95437	100.26006	3288	3.5	0.7746	19.54	0.3812	5.7 ± 0.2	7.7 ± 0.2	20.3 ± 1.4
	IAM007	44.95438	100.26004	3288	4	0.7746	18.96	0.3738	5.3 ± 0.2	7.2 ± 0.2	19.1 ± 1.3
M_{J4}	JAM001	44.97614	100.29007	3412	3	0.8218	16.91	0.3842	78.6 ± 0.6	124.9 ± 1.6	278.9 ± 18.1
	JAM002	44.97627	100.29012	3411	4	0.8218	20	0.3993	57.0 ± 0.6	79.7 ± 1.1	177.3 ± 11.3
	JAM003	44.97651	100.29021	3411	2.5	0.8218	20.03	0.3871	194.3 ± 1.2	262.9 ± 3.1	636.2 ± 45.1
	JAM004	44.97654	100.28988	3409	3	0.8218	20	0.382	70.9 ± 0.6	94.8 ± 1.3	208.9 ± 13.3
	JAM005	44.97665	100.29008	3409	2.5	0.8218	20.03	0.375	64.8 ± 0.5	84.9 ± 1.1	186.6 ± 11.8
M_{J3}	JAM006	44.97891	100.29092	3350	3	0.8363	20.02	0.3708	12.3 ± 2.6	15.9 ± 3.4	35.9 ± 8.0
	JAM007	44.97886	100.29079	3351	3	0.8363	20.03	0.3707	25.3 ± 5.0	32.8 ± 6.5	74.1 ± 15.7
	JAM008	44.97894	100.29084	3350	3	0.8363	20.42	0.3932	68.9 ± 7.0	92.9 ± 9.5	209.0 ± 26.1
	JAM009	44.97891	100.29095	3348	3.5	0.8363	19.97	0.3832	15.3 ± 2.7	20.5 ± 3.7	45.8 ± 8.7
	JAM010	44.97897	100.29089	3348	3.5	0.8363	19.97	0.3856	40.9 ± 5.7	55.2 ± 7.7	123.8 ± 19.4
M_{J2}	JAM011	44.98058	100.29328	3293	2.5	0.8598	19.91	0.3903	52.3 ± 0.5	71.7 ± 1.0	162.1 ± 10.2
	JAM012	44.98083	100.29321	3289	2	0.8598	19.97	0.3785	93.6 ± 0.6	124.2 ± 1.5	284.9 ± 18.4
	JAM013	44.98095	100.29263	3289	4	0.8598	20.22	0.3794	81.0 ± 4.1	106.4 ± 5.5	246.6 ± 20.6
	JAM014	44.98096	100.29259	3292	3	0.8598	20.38	0.3812	61.0 ± 6.4	79.9 ± 8.4	181.9 ± 23.0
	JAM015	44.98096	100.2926	3292	3	0.8598	20.04	0.3894	59.4 ± 5.2	80.8 ± 7.1	184.0 ± 20.3
M_{J1}	JAM016	44.98224	100.29684	3193	3.5	0.8852	19.91	0.3872	3.0 ± 0.1	4.0 ± 0.2	10.6 ± 0.8
	JAM017	44.98232	100.29693	3191	3	0.8852	20.05	0.3935	4.8 ± 0.3	6.6 ± 0.4	16.3 ± 1.4
	JAM018	44.98232	100.29693	3191	2.5	0.8852	20.06	0.3864	5.8 ± 0.4	7.8 ± 0.5	18.9 ± 1.7
	JAM019	44.98326	100.29745	3170	3	0.8935	20.17	0.3962	4.4 ± 0.2	6.0 ± 0.3	15.1 ± 1.3
	JAM020	44.98379	100.29716	3172	3.5	0.9311	20.14	0.3865	5.8 ± 0.2	7.7 ± 0.2	18.2 ± 1.2
	JAM021	44.98385	100.29712	3171	3	0.9311	20.04	0.3879	5.4 ± 0.2	7.3 ± 0.2	17.4 ± 1.2

[a] Sampling thickness of the boulders' outermost exposed surfaces.
[b] Topographic shielding factors for each sampling site were measured at intervals of 30°.
[c] Weight of the pure quartz. The density of granite (2.7 g cm^{-3}) was used to calculate exposure age.
[d] A mean value of process blank samples (4.53 x 10^{-15} ± 1.62 x 10^{-15}) was used for correction.

1067   [e] Ratios of $^{10}Be/^9Be$ were normalized with 07KNSTD reference sample 5-1 prepared by Nishiizumi et al. (2007) with
1068   a $^{10}Be/^9Be$ ratio of $2.71\times10^{-11} \pm 4.71\times10^{-13}$ (calibrated error) and using a ^{10}Be half-life of 1.36×10^6 years (Chmeleff
1069   et al., 2010; Korschinek et al., 2010)
1070   [f] Uncertainties were calculated at the 1σ confidence level.
1071   [g] Exposure ages, assuming zero erosion were calculated using CRONUS-Earth online calculator version 3.0.2 (Balco
1072   et al., 2008).
1073   [h] Constant production rate of the ^{10}Be model of Stone (2000) was used for calculating exposure age.
1074   [i] Constant production rate of the ^{10}Be model of Lifton et al. (2014) was used.
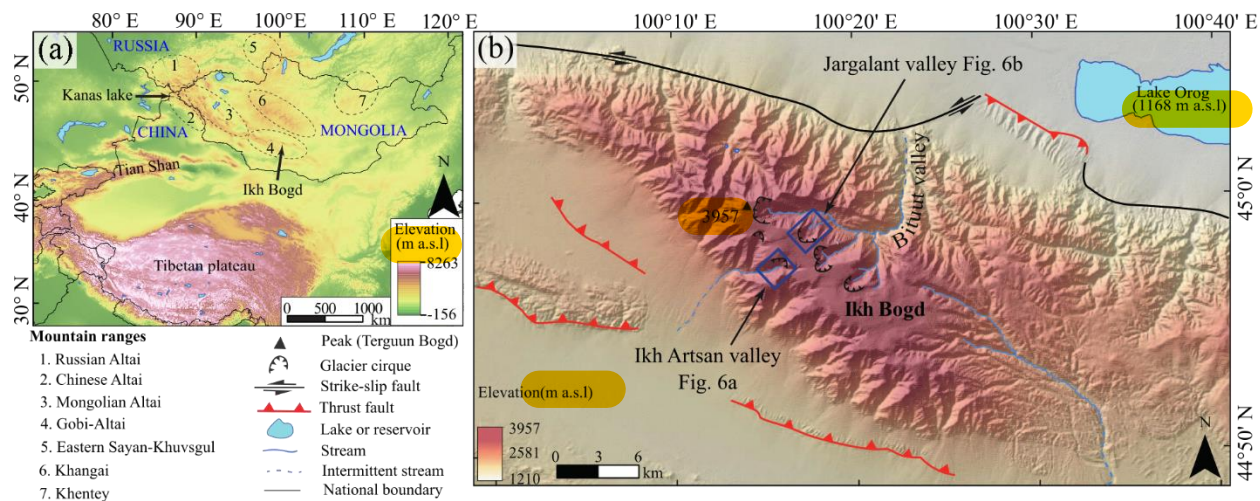
Fig. 1. Study area. (a) Central Asian glaciated mountain ranges during late Quaternary. (b) Study area. Boxed areas indicate Ikh Artsan and Jargalant valleys. See the detailed maps of both valleys visualized in Figs. 4-6. The background image is shaded SRTM DEM with 30 m resolution.

1080
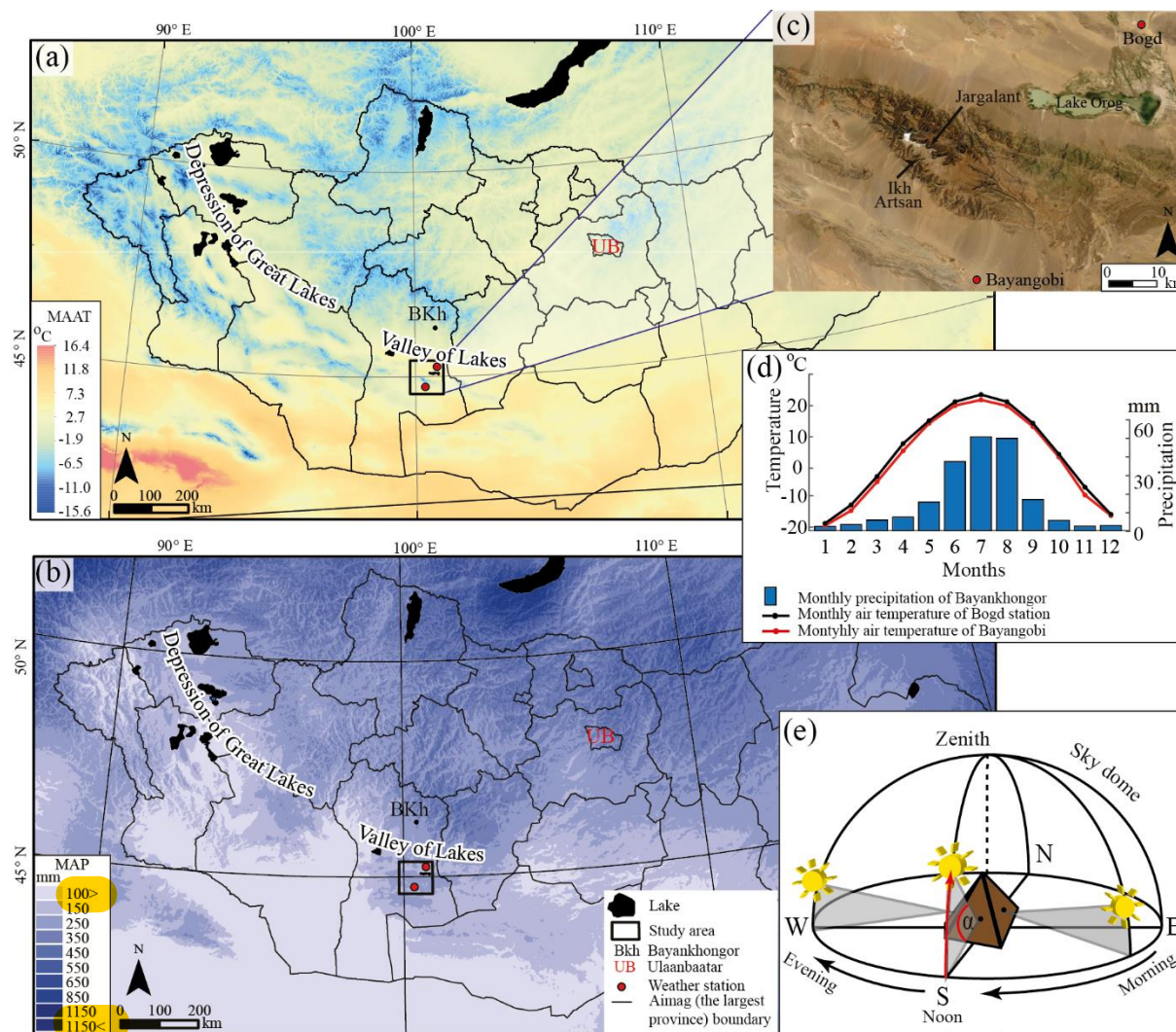
Fig. 2. The present-day climate of Mongolia. (a) Mean annual air temperature across Mongolia. (b) Mongolian mean annual precipitation. BKh (black dot) represents Bayankhongor aimag (the largest unit of province) center, and UB is Ulaanbaatar, the capital of Mongolia. Red dots mark the nearest weather stations to the study area. Temperature data (CHELSA_Bio10_01, at 30 arc-second) and precipitation data (CHELSA_Bio10_12, at 30 arc-second) are long-term (1973-2013) annual means. Source: Bioclim Bio1 data, CHELSA V 1.2 (Karger et al., 2017). (c) The exact locations of the nearest weather stations to the massif, Bayangobi (1540 m a.s.l) and Bogd (1240 m a.s.l). (d) Long-term (1989-2019) monthly mean temperature from Bogd station (black graph) and Bayangobi station (red graph). Monthly mean precipitation (2005-2019) of Bayankhongor is described as blue bar chart (NAMHEM, 2020). (e) Solar altitude angles on the mountain slopes with different aspect. Solar altitude angles (α) at different hour angles (morning to evening). Solar altitude angle is 0 degree at sunrise and reaches its maximum value at noon. In the mountainous area of northern hemisphere, south-facing slope receives highest energy at noon, however, north-facing slope receives less or no energy due to topographic shading effect.
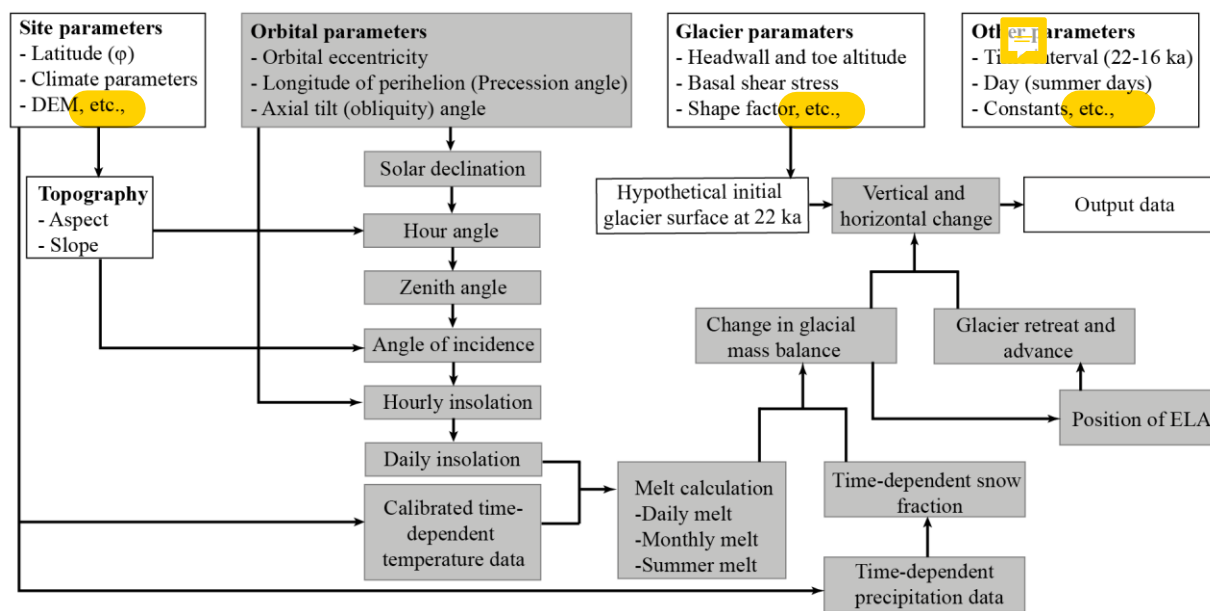
1093

1094   **Fig. 3.** Source code structure diagram of 2D ice surface modelling
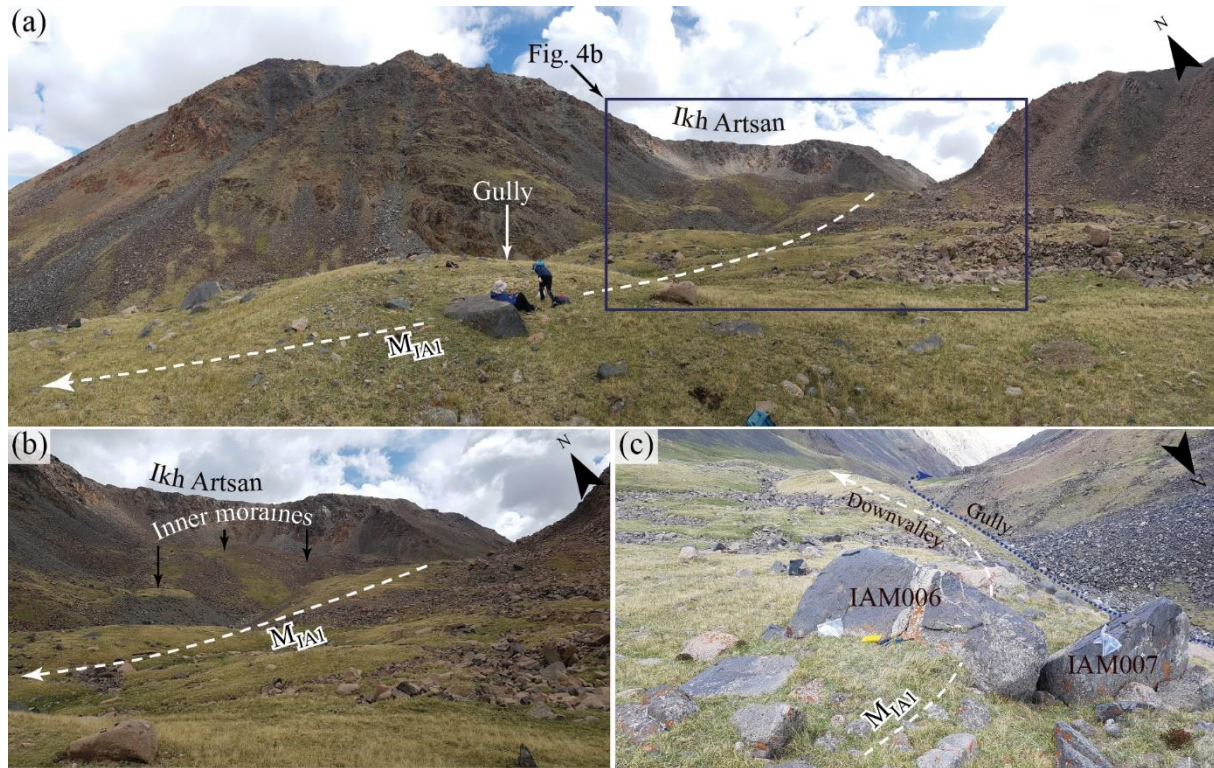
1095

Fig. 4. Photo composites of the Ikh Artsan valley and paleoglacial evidence. (a) Ikh Artsan glacial cirque and distal moraine ridge. The white dashed arrow represents M_{IA1} moraine ridge, which marks the farthest extent of late Quaternary glaciation. (b) Distal and inner moraine sequences (Batbaatar et al., 2018). (c) IAM006 and IAM007 sampling boulders are on the M_{IA1} moraine ridge.

1100

Fig. 5. Geomorphologic setting and moraine stratigraphy in Jargalant valley. (a) Jargalant valley and Bituut trunk valley that extends from the cirque near the highest peak (3957 m a.s.l). Jargalant valley is one of the large tributaries of Bituut valley, while covered by a large amount of late Quaternary moraine complex. (b) The stratigraphic boundary between M_{J4} and M_{J3} moraines in the Jargalant cirque. Moraines are dissected by longitudinal gullies. (c) Pair of M_{J2} moraine and oldest M_{J1} moraine ridge. Horses (red circle) are for scale. (d) Boulder sizes on M_{J2} moraine range from sub-meter to several meters. (e) Downvalley view of the moraine sequences from the uppermost moraine sequence.

1107
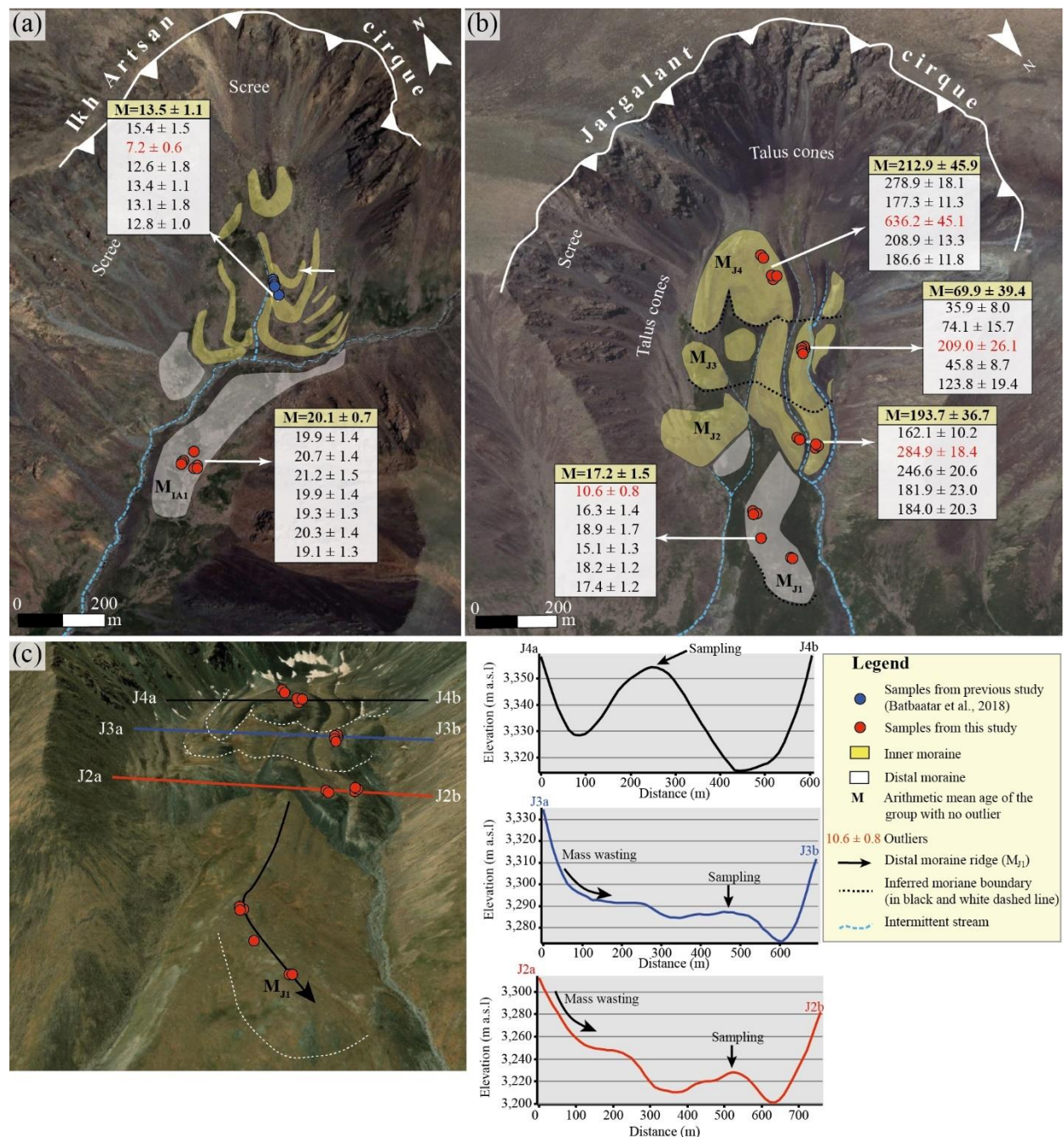
1108

1109 **Fig. 6.** [10]Be Exposure ages (ka) for outer (white) and inner (yellow) moraine sequences. (a) Exposure ages from Ikh
1110 Artsan moraine sequences. (b) Age dating result of Jargalant hummocky moraine complex. Background images of (a)
1111 and (b) are © Bing Maps (2023) aerial imageries. (c) Cross-section view of inner moraine sequences (M$_{J4}$ ~ M$_{J2}$) of
1112 Jargalant valley. Background image is oblique imagery of © ArcGIS Earth (2023) V1.16.0.3547. Mass wasting
1113 deposits on the moraine surface and intermittent stream incision have altered the original moraine morphologies.
1114 Samples were taken from the highest intact point of the longitudinally elongated moraine ridge, which thought to be
1115 unaffected by reworking processes. Since the exposure age dating result from inferred inner moraine sequences (M$_{J4}$
1116 ~ M$_{J2}$) shows high inheritance, which cannot contribute the inferred moraine sequences.
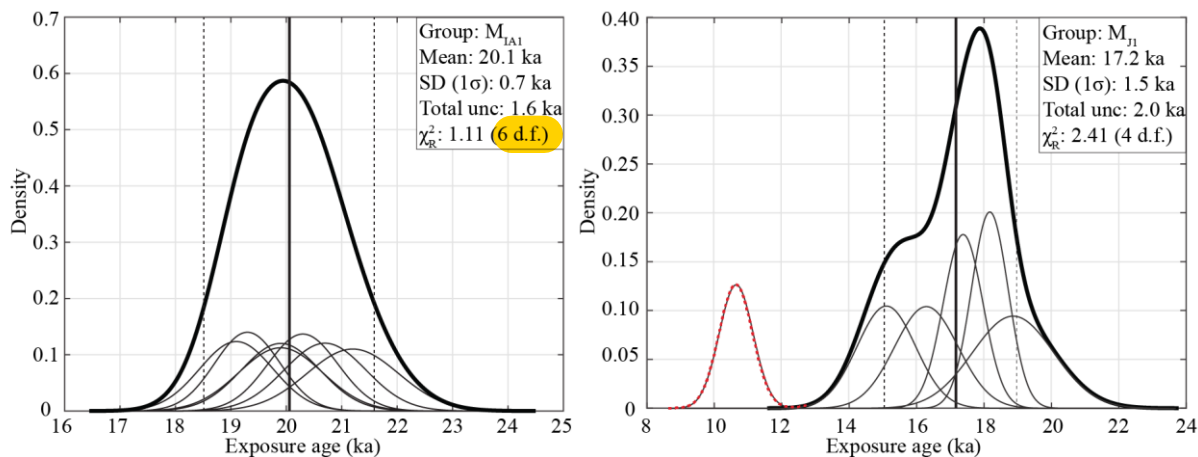
1117

1118 **Fig. 7.** Kernel density plot (KDP) of estimated [10]Be exposure ages from distal moraine crests in Jargalant and Ikh
1119 Artsan valleys. Plots were created using IceTEA Matlab code by Jones et al. (2019). (a) KDP of exposure ages of the
1120 most extensive moraine sequence (M_{IA1}) in Ikh Artsan valley. No outlier was detected. The arithmetic mean was
1121 calculated and marked as a bold solid vertical line. (b) KDP of exposure ages from the oldest (M_{J1}) moraine sequence
1122 in Jargalant valley. The outlier was excluded by Chauvenet, Pierce, and the standardized deviation method in the 1
1123 sigma range. The thick solid lines represent the cumulative density curve, the dashed red line shows excluded outlier,
1124 and solid, narrow black lines show individual density curves for each sample. The range of total uncertainty of the
1125 group is marked as two vertical dashed lines. The sample statistics were calculated after rejecting outliers, while
1126 internal errors were used to create KDP and calculate sample statistics.
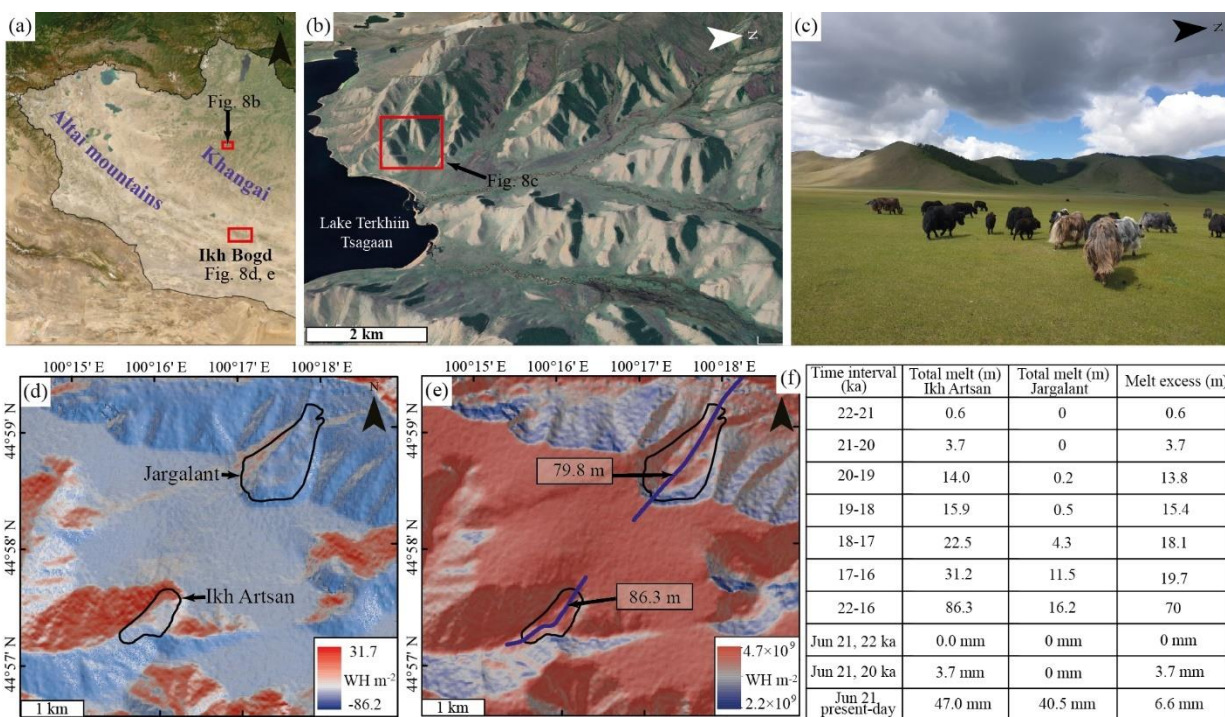
Fig. 8. Asymmetric distribution of potential clear-sky direct solar radiation, glacial melt, and vegetation on the south- and north-facing slopes. (a) Location map of Ikh Bogd and lake Terkhiin Tsagaan. (b, c) Tree distribution on north-facing slope, north of lake Terkhiin Tsagaan (© Google Earth 2022; photo taken by authors). (d) Anomaly of total clear-sky direct solar radiation of June solstice in 20 ka from modern value. (e) Integrated total summer insolation for 22-16 ka. The purple line represents profile along midline in Ikh Artsan and Jargalant valley. Integrated total melt was calculated in Ikh Artsan as 86.3 m and 79.8 m in Ikh Artsan valley for 22-26 ka at the same temperature. (f) Integrated total melt calculation for Ikh Artsan and Jargalant valley considering average summer temperature in Jargalant is 0.5 lower than that in Ikh Artsan.
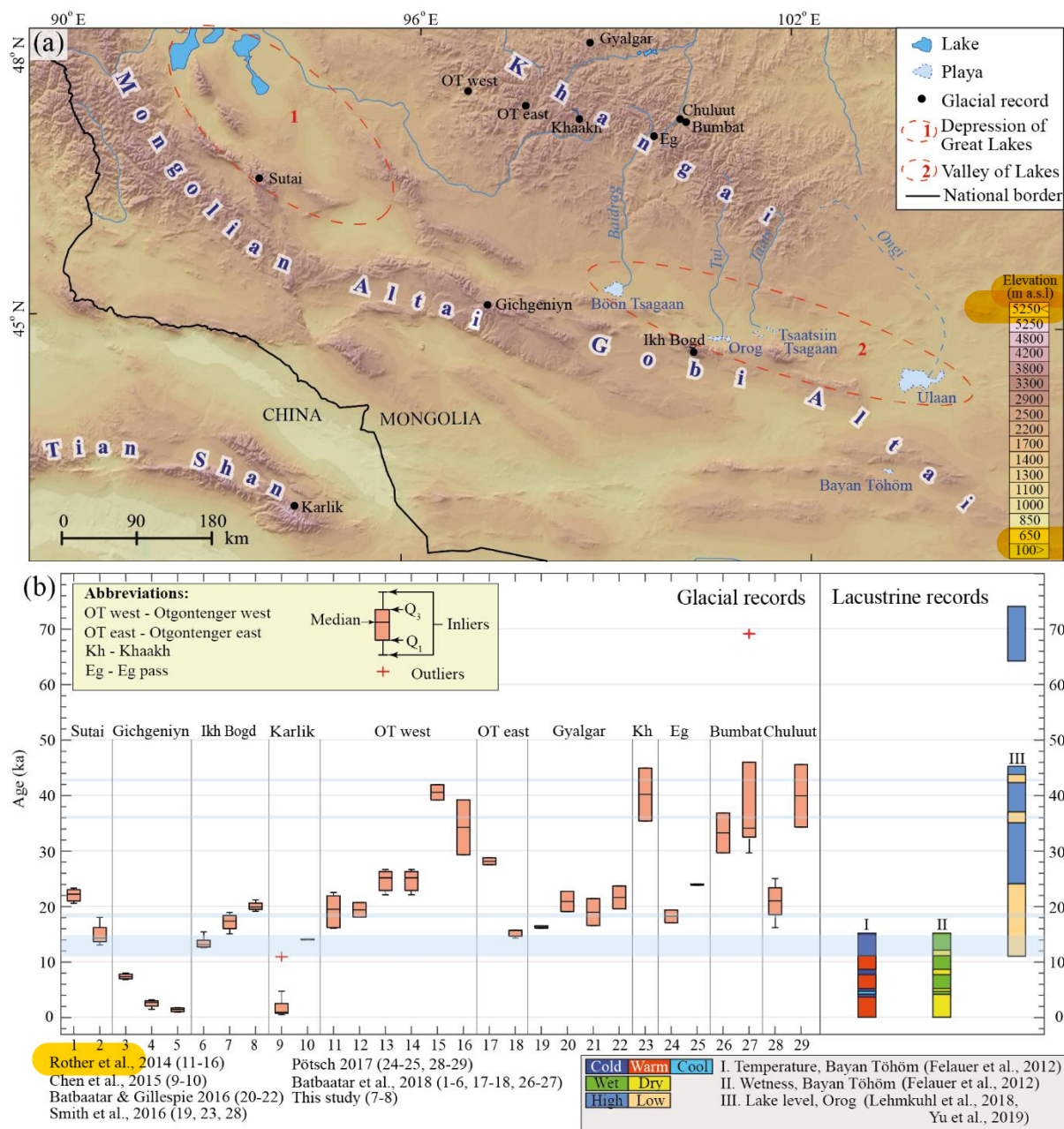
148

Fig. 9. Temporal and spatial distributions of glacial and paleo-lacustrine records in the neighboring regions of Ikh
Bogd massif. (a) Locations of the ^{10}Be age dating sites for paleoglaciers and paleo lacustrine proxies. (b) Age dating
results from glaciers and lacustrine proxies. Glacial records on the left are the ^{10}Be exposure age dating results
representing 29 individual moraine groups. Exposure ages were recalculated with Cronus Earth V3, using the LSDn
scaling factor (Lifton et al., 2014). Only effective ages were plotted after outlier rejection using the Chauvenet, Peirce,
and normalized deviation method. On each box, central mark indicates the median, and the bottom and top edges of
the box indicate the 25th (Q$_1$) and 75th (Q$_3$) percentiles, respectively. The whiskers extend only to the data points
considered inliers, and the additional outliers were detected from the effective ages and plotted individually using the
'+' marker symbol. The shaded light blue sections on the age interval present the major harsh periods (playa phase of
Orog, Yu et al., 2019). Lacustrine records on the right present temperature (I) and wetness data (II) in lake Bayan
Töhöm and lake level record of lake Orog (III).

1149

22.0 21.5 20.5 20.0 17.1 ka Ice surface profile and corrsponding timing of advancing glaier

19.5 ka Ice surface profile and corresponding timing of retreating glacier
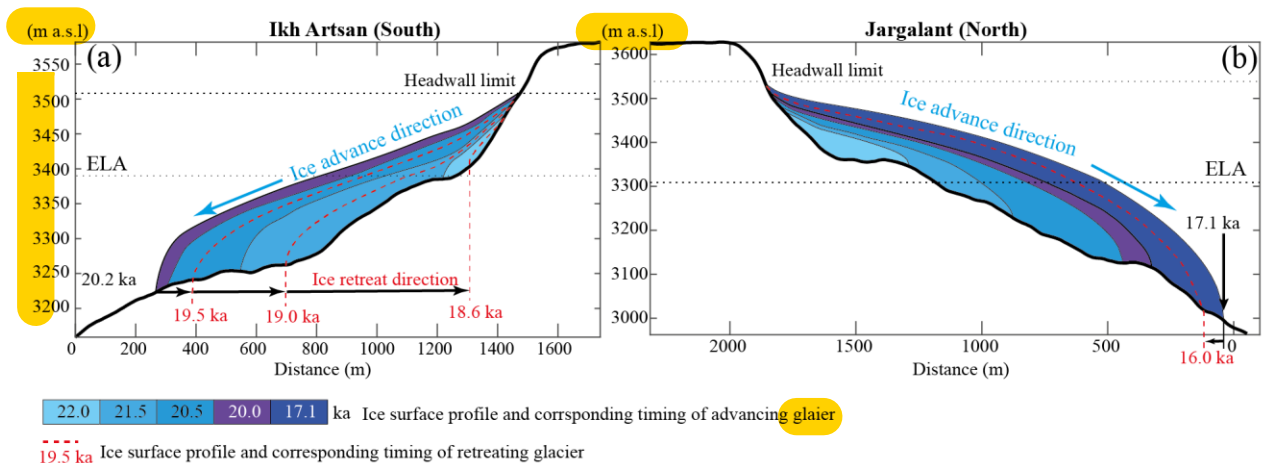
1150

1151 **Fig. 10.** Asynchronous advance and retreat pattern of Ikh Bogd paleoglacier during 22-16 ka. (a) Paleoglacier in Ikh
1152 Artsan valley advanced between 22.0 and 20.2 ka and retreated from 20.2 to 18.6 ka. (b) Paleoglacier in Jargalant
1153 valley most expanded downvalley between 22.0 and 17.1 ka. Small retreat is observed during 17.1-16.0 ka. The
1154 present-day summer temperature in the north-facing valley was considered 0.5 °C lower than in the south-facing valley.
1155 The present-day temperature is calibrated to Greenland (NGRIP) paleotemperature data (Buizert et al., 2018) using
1156 an LGM summer temperature anomaly of -5.5 °C. Headwall altitudes of the LGM paleoglaciers were used to mark
1157 the maximum thickness of the glacier.
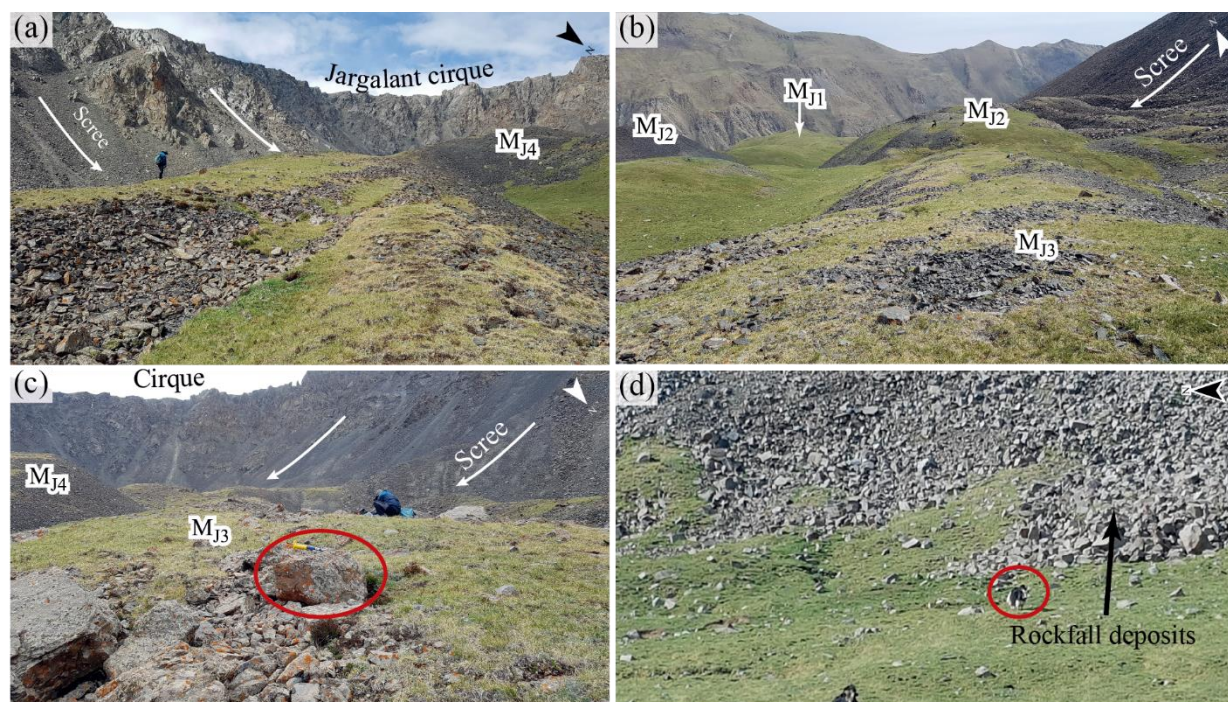
1158

1159 **Fig. 11.** Rockfall deposits in Jargalant valley. The scree or talus cone was on the cirque wall. M_{J4}, M_{J3}, and M_{J2}
1160 moraine formed within a Jargalant cirque, consequently outer edges of moraine ridges near the cirque wall were
1161 covered with talus deposit. (a) Rockfall deposit on the southeastern cirque wall, near M_{J4} moraine. (b) Scree covering
1162 on M_{J2} moraine that is dissected by an intermittent stream. (c) Sampling site of M_{J3} moraine and scree on the southern
1163 and southwestern wall of the cirque, near M_{J4}, M_{J3} moraine. JAM010 was taken from the circled boulder. Chisel, for
1164 scale, is on the boulder. (d) Rockfall deposit on the eastern slope of the cirque. Yak (circled) is for scale.

1165
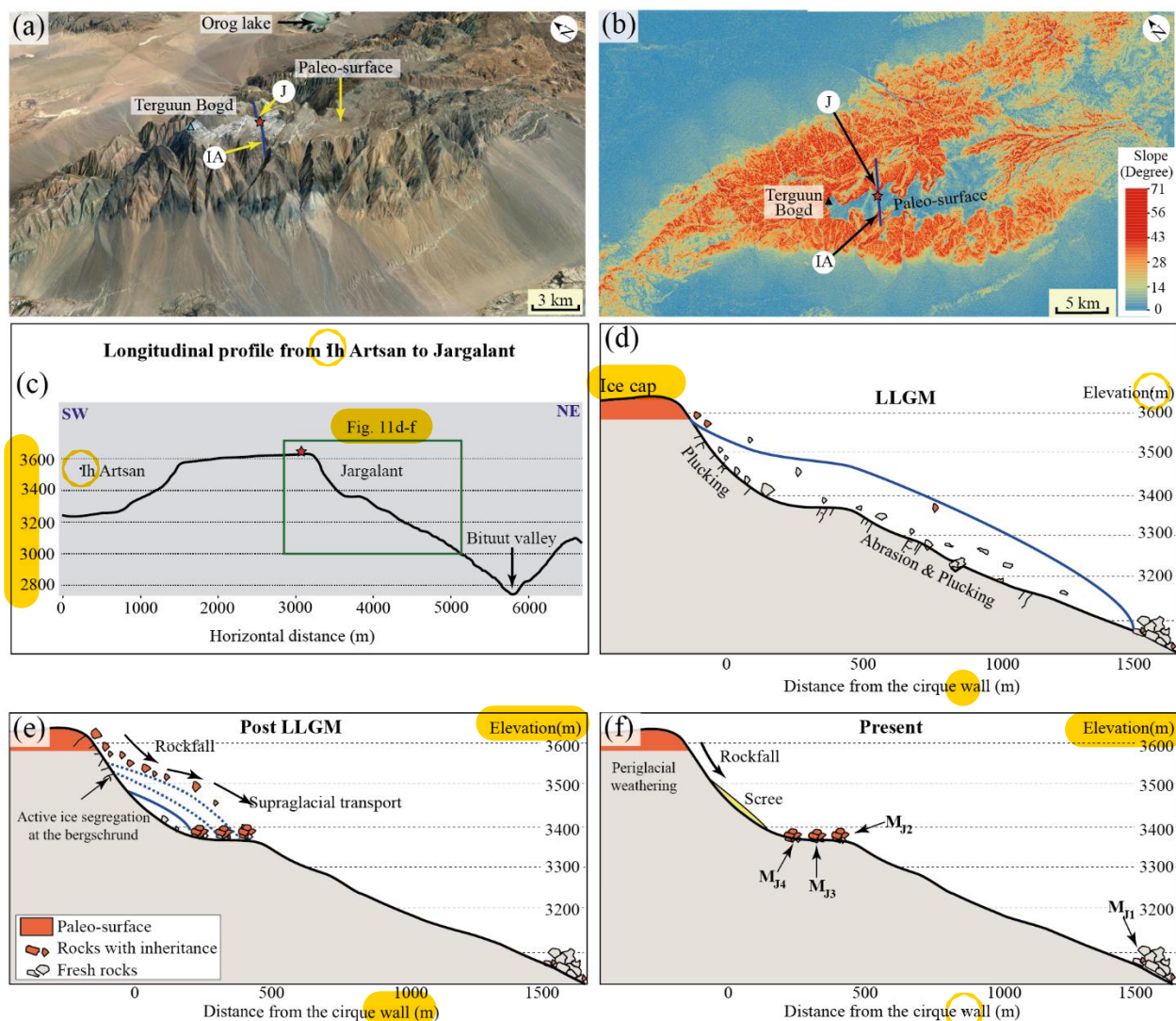
1166

Fig. 12. Inheritance from the uplifted paleo-surface of Ikh Bogd massif. (a) 3D view of the paleo-planation surface (© Google Earth, 2022). (b) Slope map of Ikh Bogd, location of the Ikh Artsan (IA) and Jargalant (J) valley. The green triangle represents the highest peak of the massif, Terguun Bogd. Exposure age and erosion rate (Table 2) were calculated using the highest concentration of the boulder from M_{J4}-M_{J2} (Fig. 11a) for the point location marked as red star (Fig. 11b; 3625 m). (c) Longitudinal profile along a dark blue line (See Fig. 11b) connecting Ikh Artsan and Jargalant valley from SW to NE. (d) LLGM (Local LGM ~17 ka) glacial extent. Plucking of fresh rocks was intensive due to glacial length and thickness. (e) Enhanced supply of highly inherited rocks into M_{J4}, M_{J3}, and M_{J2} moraine series which are formed by successive glacial advances or/and stagnation. According to a shortage of glacier length, low number of fresh rocks are plucked out. Thinned glacier allows intensive ice segregation along the bergschrund and more inherited rockfalls into the ice surface. Hence, boulder supply with inheritance of paleo surface would increase. (f) Present-day rockfall deposit without supraglacial transport.